Geophysical Journal International

Geophys. J. Int. (2017) **211,** 400–417
Advance Access publication 2017 July 27
GJI Seismology

doi: 10.1093/gji/ggx312

Simulation of broad-band strong ground motion for a hypothetical M_w 7.1 earthquake on the Enriquillo Fault in Haiti

Roby Douilly,[1] George P. Mavroeidis[2] and Eric Calais[3]

[1]*Department of Earth Sciences, University of California, Riverside, Riverside, CA* 92521, *USA. E-mail:roby.douilly@ucr.edu*
[2]*Department of Civil and Environmental Engineering and Earth Sciences, University of Notre Dame, Notre Dame, IN* 46556, *USA*
[3]*Department of Geosciences, École Normale Supérieure, PSL Research University, F-*75005 *Paris, France*

Accepted 2017 July 26. Received 2017 July 23; in original form 2016 December 16

SUMMARY

The devastating 2010 M_w 7.0 Haiti earthquake demonstrated the need to improve mitigation and preparedness for future seismic events in the region. Previous studies have shown that the earthquake did not occur on the Enriquillo Fault, the main plate boundary fault running through the heavily populated Port-au-Prince region, but on the nearby and previously unknown transpressional Léogâne Fault. Slip on that fault has increased stresses on the segment of Enriquillo Fault to the east of Léogâne, which terminates in the ∼3-million-inhabitant capital city of Port-au-Prince. In this study, we investigate ground shaking in the vicinity of Port-au-Prince, if a hypothetical rupture similar to the 2010 Haiti earthquake occurred on that segment of the Enriquillo Fault. We use a finite element method and assumptions on regional tectonic stress to simulate the low-frequency ground motion components using dynamic rupture propagation for a 52-km-long segment. We consider eight scenarios by varying parameters such as hypocentre location, initial shear stress and fault dip. The high-frequency ground motion components are simulated using the specific barrier model in the context of the stochastic modeling approach. The broad-band ground motion synthetics are subsequently obtained by combining the low-frequency components from the dynamic rupture simulation with the high-frequency components from the stochastic simulation using matched filtering at a crossover frequency of 1 Hz. Results show that rupture on a vertical Enriquillo Fault generates larger horizontal permanent displacements in Léogâne and Port-au-Prince than rupture on a south-dipping Enriquillo Fault. The mean horizontal peak ground acceleration (PGA), computed at several sites of interest throughout Port-au-Prince, has a value of ∼0.45 g, whereas the maximum horizontal PGA in Port-au-Prince is ∼0.60 g. Even though we only consider a limited number of rupture scenarios, our results suggest more intense ground shaking for the city of Port-au-Prince than during the already very damaging 2010 Haiti earthquake.

Key words: Earthquake dynamics; Earthquake ground motions; Earthquake hazards.

1 INTRODUCTION

Global positioning system (GPS) measurements have shown that the Caribbean plate is currently moving at about 2 cm yr^{-1} with respect to the North American plate (DeMets *et al.* 2000). This relative motion is distributed across two major active faults in Hispaniola, the Septentrional Fault (SF) along the northern coast of the island and the Enriquillo Plantain Garden Fault (EPGF) that cuts through the southern peninsula of Haiti (Fig. 1). Historical records document large seismic events in the vicinity of these two strike-slip faults in 1701, 1751, 1770, 1842 and 1887 (Scherer 1912). These events may have ruptured segments of the SF and the EPGF (Fig. 1, Ali *et al.* 2008; Bakun *et al.* 2012) or may have occurred on nearby faults.

GPS measurements in Hispaniola prior to the 2010 Haiti earthquake showed that the EPGF, presumed to have last ruptured ∼250 yr ago, had accumulated sufficient elastic strain to generate an M_w 7.2 earthquake if all of that energy were to be released in one event (Manaker *et al.* 2008). Therefore, the 2010 M_w 7.0 Haiti earthquake was originally thought to result from the rupture of an EPGF segment. However, subsequent studies showed that more than 80 per cent of the moment release occurred on a different fault, dipping to the north under the heavily affected city of Léogâne (Calais *et al.* 2010; Hayes *et al.* 2010; Mercier de Lépinay *et al.* 2011; Meng *et al.* 2012; Douilly *et al.* 2013, 2015; Symithe *et al.* 2013). Therefore, the EPGF, which did not rupture in 2010, remains a prime candidate for future earthquakes in the region. Furthermore, it cannot be excluded that the 2010 main shock marks the beginning of cascade-like events similar to the Landers earthquake sequence in southern California (Hauksson *et al.* 1993) or the migrating seismic events along the North Anatolian Fault in Turkey (Stein *et al.* 1997; King *et al.* 2001).

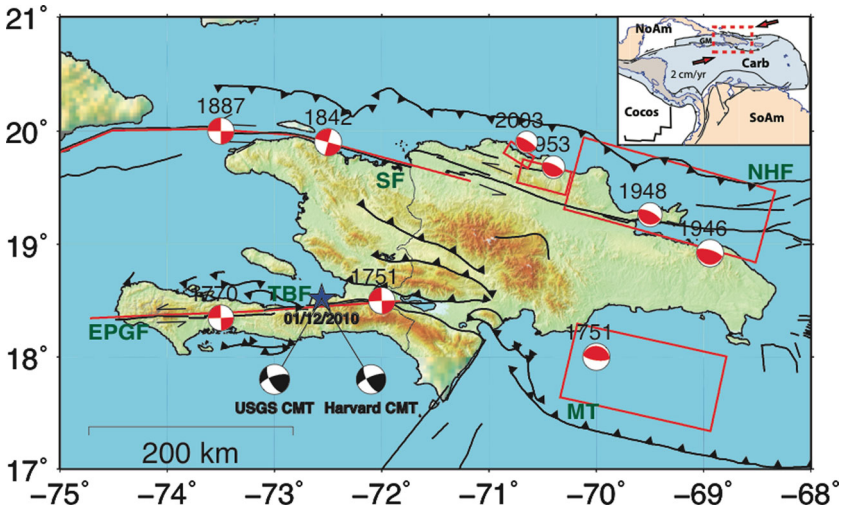

Figure 1. Map showing the tectonic context of the Hispaniola Island. The red focal mechanisms are historical earthquakes along with the surface projection of their rupture planes. The USGS and Harvard CMT focal mechanisms are displayed in black. North Hispaniola Fault, NHF; Enriquillo Plantain Garden Fault, EPGF; Trois Baies Fault, TBF; Septentrional Fault, SF and Muertos Trough, MT. Inset: location of the Caribbean plate (CARB) with respect to the North American plate (NoAm), South American plate (SoAm) and Cocos plate. The red dashed box encloses the Hispaniola Island and the arrows indicate the relative motion of the Caribbean plate with respect to the North American plate.

Under the current state of knowledge, although the occurrence of earthquakes cannot be predicted, one can estimate the amplitude, duration, frequency content and spatial variability of the ground motion that is likely to occur at a particular site during an earthquake. This is achieved by modeling probable earthquake scenarios using deterministic (kinematic or dynamic) and/or stochastic ground motion simulation techniques. An example of rupture scenario likelihood based on dynamic rupture simulations is the segmented Middle Durance Fault in southeastern France (Aochi *et al.* 2006). In that study, Aochi *et al.* (2006) studied rupture interactions among several fault segments by varying parameters such as stress field orientation and hypocentre location. The authors estimated which segments are more likely to rupture and evaluated the probability for a multisegment rupture to generate a larger event. Another example based on dynamic rupture simulations is the North Anatolian Fault in Istanbul (Aochi & Ulrich 2015), where the authors varied the fault geometry, background stress and hypocentre location. In general, kinematic or dynamic simulations are applicable to lower frequencies only. Since peak ground accelerations (PGAs) and spectral accelerations are primarily associated with high frequencies, hybrid simulation approaches that combine deterministic and stochastic simulation techniques are commonly used in practice to generate broad-band ground motions for engineering applications and advance our understanding of seismic hazard for a particular site or region (e.g. Mavroeidis *et al.* 2008; Graves & Pitarka 2010; Mai *et al.* 2010; Mavroeidis & Scotti 2013; Lozos *et al.* 2015). For example, the Southern California Earthquake Center (SCEC) has recently put together the SCEC Broadband Platform, an open-source software system that can generate broad-band ground motions for historical and scenario earthquakes using physics-based models (Goulet *et al.* 2015).

The main objective of this study is to investigate the ground shaking level in southern Haiti if a hypothetical seismic event, similar in magnitude to the 2010 M_w 7.0 Haiti earthquake, occurred on the EPGF segment adjacent to the Léogâne Fault and close to the capital city of Port-au-Prince. To achieve this objective, we use a hybrid simulation approach that combines dynamic rupture simulations at low frequencies with stochastic simulations at high frequencies.

Table 1. List of stations and their NEHRP site classification.

Station name	Station code	Longitude (°)	Latitude (°)	Soil type
Aeroport	APP	−72.291	18.579	C
Carrefour	CFR	−72.351	18.529	C
Port-au-Prince	PAP	−72.346	18.545	D
Cite-Militaire	CIM	−72.316	18.563	D
Frere	FRE	−72.270	18.525	C
Tete-de-l'Eau	TDE	−72.280	18.501	A–B
Fouche	FUC	−72.734	18.422	C
Gressier	GRS	−72.529	18.538	C
Léogâne	LEO	−72.633	18.511	D
Petit-Goave	PGv	−72.861	18.431	C
Trois Palmiste	TPM	−72.652	18.348	C
Near Fault 1	NF1	−72.617	18.442	C
Near Fault 2	NF2	−72.561	18.491	C
Near Fault 3	NF3	−72.494	18.451	C
Near Fault 4	NF4	−72.443	18.498	C
Near Fault 5	NF5	−72.373	18.473	C
Near Fault 6	NF6	−72.188	18.528	C
Cannaan	CAN	−72.251	18.659	C
Zoranger	ZOR	−72.319	18.633	C
Bureau of Mines	HBME	−72.297	18.563	C
LaBoule	HCEA	−72.305	18.504	A–B
Hotel Montana	HHMT	−72.297	18.527	C
Killick	HPKH	−72.380	18.533	C
Plaza Hotel	HPLZ	−72.330	18.540	C
Voila Canapevert	HVCV	−72.309	18.529	C
Voila SLG	HVGZ	−72.304	18.553	C
Voila Pont Rouge	HVPR	−72.38	18.563	D
US Embassy Tabarre	USEM	−72.249	18.565	C

We analyse a range of rupture scenarios on the considered EPGF segment and generate synthetic ground motions at 19 hypothetical stations and 9 locations where portable K2 accelerometers were deployed following the 2010 Haiti earthquake (Table 1 and Fig. 2) (Hough *et al.* 2010). These accelerometers were installed in the near field of the rupture with their locations chosen based on the geological setting of the Port-au-Prince metropolitan area (Cox *et al.* 2011; Gilles *et al.* 2013; St Fleur *et al.* 2016). It is anticipated that

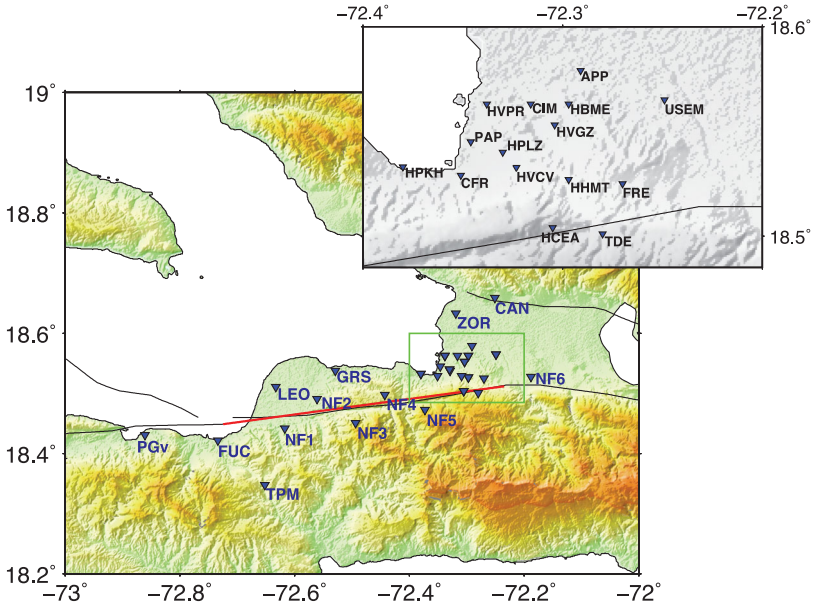

Figure 2. Map showing the distribution of hypothetical stations selected for the simulation of broad-band ground motions. The red line represents the segment of the EPGF modeled in this study.

the findings of this study will help assess the seismic hazard in the region.

2 TECTONIC SETTING

The EPGF is a long strike-slip fault that marks the boundary between the Gonave microplate and the Caribbean plate from Jamaica to southern Hispaniola (Mann *et al.* 1991, 1995; Mann & Gordon 1996). In the southern peninsula of Haiti, the EPGF consists of three distinct strands (western, central and eastern). The western one cuts through the peninsula from Tiburon to Petit-Goâve, whereas the central one extends from Léogâne to Port-au-Prince. These two strands are well expressed in the land surface morphology of the region (Calmus 1983; Momplaisir 1986; Mann *et al.* 1995). Along the central one, Prentice *et al.* (2010) found geomorphic evidence for either vertical or south-dipping faulting with an average dip angle of 65°. The authors also measured left-lateral offset streams along a 12-km-long fault segment, which they interpreted to result from left-lateral slip during the 1751 or 1770 events.

The eastern strand, which runs from the Cul-de-Sac Basin to the Dominican Republic, is less well expressed in the morphology. Mann *et al.* (1995) interpreted it as a vertical left-lateral fault, whereas early geological work in southern Haiti mapped the southern boundary of the Cul-de-Sac Basin as a south-dipping reverse fault (Bourgueil *et al.* 1988). Recent geological studies, showing active reverse-sinistral faults in the Cul-de-Sac Basin (Terrier *et al.* 2014; Saint Fleur *et al.* 2015) and geodetic evidence for north–south shortening localized along the southern edge of the basin (Symithe & Calais 2016), are consistent with the latter hypothesis.

Historical records report four large-magnitude events in southern Hispaniola in the past ∼500 yr, all of them in the 18th century (Scherer 1912). Their magnitude and location were estimated by Bakun *et al.* (2012) on the basis of the damage reported in historical archives: 1701, intensity magnitude M_I 6.6, close to the 2010 Haiti earthquake; 1751 October 18, M_I 7.4, southern Dominican Republic; 1751 November 21, M_I 6.6, near Port-au-Prince; and 1770 June 3 M_I 7.5, west of the 2010 Haiti earthquake. In addition, geological mapping of the active EPGF in the Southern Peninsula of Haiti shows that its eastern strand consists of four segments of ∼50 km length (Saint Fleur *et al.* 2015), each capable of an M_w 7 earthquake (Wells & Coppersmith 1994).

In our analysis, we chose to consider the central strand of the EPGF because of its proximity to the heavily populated city of Port-au-Prince and because its length (∼52 km) and single-segment geometry make it a candidate for a future M_w 7.0 earthquake in the region. The geometry of this segment (Fig. 2) is consistent with either interpretation of the eastward continuation of the EPGF into the Cul-de-Sac Basin discussed previously. Finally, that the central strand of the EPGF has been pushed closer to failure by the 2010 earthquake (Symithe *et al.* 2013; Douilly *et al.* 2015) is yet another justification for investigating a rupture scenario on this fault segment. Fault segmentation and historical earthquakes indicate that this scenario is a realistic one for the region, although not the worst case as several segments could rupture in a single event with a magnitude significantly larger than M_w 7.0.

3 SYNTHESIS OF LOW-FREQUENCY GROUND MOTION USING DYNAMIC RUPTURE MODELING

3.1 Faulting model and numerical scheme

In agreement with the tectonic setting described in Section 2, we consider two hypothetical fault geometries—a vertical plane and a plane dipping to the south at 65°. The strike and length of both faults are consistent with fault trace information published in the literature (Mann *et al.* 1995). We use CUBIT (available at: http://cubit.sandia.gov) to generate a finite element model that is 150 km long, 200 km wide and 100 km deep, centred at (18.5°, −72.5°). We discretize the model space using tetrahedral elements with dislocation across the fault surface. As in Douilly *et al.* (2015), we choose the mesh size to be 250 m on the fault and to grow geometrically away from the fault at a rate of 1.03^n, where n is an integer that depends on the hypocentral distance from any point inside the medium to the closest point on the fault plane. We

Table 2. Crustal model for dynamic rupture simulations (from Douilly *et al.* 2013).

Depth range (km)	*P*-wave velocity (km s^{-1})	*S*-wave velocity (km s^{-1})	Density (kg m^{-3})
0.0–4.0	5.28	2.76	2500
4.0–6.0	5.36	2.86	2600
6.0–9.0	5.78	3.10	2700
9.0–20.0	6.50	3.61	2800
20.0–25.0	7.01	4.15	3000
25.0–	7.30	4.27	3300

incorporate the resulting mesh into PyLith version 1.9 (Aagaard *et al.* 2013; Douilly *et al.* 2015) to carry out the dynamic rupture simulation. We use a semi-infinite layered elastic medium with a 1-D structure (Table 2), derived from the 1-D velocity model of Douilly *et al.* (2013). We allow a total dynamic simulation time of 60 s with a time step interval of 0.01 s.

3.2 Stress field and frictional parameters

In the absence of regional stress studies for Haiti that would provide the optimum direction of the stress axes, Douilly *et al.* (2015) used a trial-and-error approach to estimate the direction of the principal stress that could generate shear stresses consistent with the expected motion on the Léogâne, Enriquillo and Trois Baies fault segments together, under the assumption that the slip vector is colinear with the direction of the shear traction (Angelier 1979; Gephart & Forsyth 1984). They found a maximum horizontal stress orientation between N50°E and N60°E.

In this work, we apply the same procedure, but only the N50°E orientation is considered to estimate the initial state of stress on the EPGF. This is consistent with principal strain rates derived from a recent compilation of geodetic results in the region (Calais *et al.* 2016). Similar to Douilly *et al.* (2015), we estimate the principal strain components using the shape factor R and relate them to the principal stress components as shown in eq. (1) (Angelier 1990; Aagaard *et al.* 2004):

$$R = \frac{\varepsilon_1 - \varepsilon_2}{\varepsilon_1 - \varepsilon_3} \text{ where } \varepsilon_1 = 6 \times 10^{-4} \text{ and } \varepsilon_2 = 1 \times 10^{-4}$$

$$\begin{bmatrix} \sigma_1 \\ \sigma_2 \\ \sigma_3 \end{bmatrix} = \begin{bmatrix} \lambda + 2\mu & \lambda & \lambda \\ \lambda & \lambda + 2\mu & \lambda \\ \lambda & \lambda & \lambda + 2\mu \end{bmatrix} \begin{bmatrix} \varepsilon_1 \\ \varepsilon_2 \\ \varepsilon_3 \end{bmatrix} \quad (1)$$

where ε is the estimated principal strain tensor, σ is the principal stress tensor and λ and μ are the Lamé parameters. Because of the uncertainty in the stress field, the principal stress tensor is estimated at an average depth of 8 km in order to have a uniform shear and normal stress across the fault. The principal stress is rotated to the east-north-up coordinate system and a constant overburden pressure is added to the normal stresses to prevent the fault from opening. The resulting stress tensor is then used to calculate the initial shear and normal tractions on the fault plane. As a result, these initial tractions are different for the vertical and south-dipping fault cases. We should also note that the principal stress orientation and magnitude used in this study are not well constrained because there is no prior stress inversion study for this region. Therefore, varying the orientation of the principal stresses will impact the magnitude of the shear and normal tractions.

In source dynamics, traction and slip on a fault are related through a friction law. In this study, the slip-weakening friction law (Ida 1972; Andrews 1976) is adopted, where fault slip is considered to be zero until the shear stress reaches a critical value. The shear stress then decreases linearly from the failure stress to the sliding stress along a slip-weakening distance (D_c). This fracture criterion is expressed by the friction coefficient μ_f:

$$\mu_f = \begin{cases} \mu_d + \left(1 - \frac{D}{D_c}\right)(\mu_s - \mu_d) & \text{if } D \le D_c \\ \mu_d & \text{if } D > D_c \end{cases} \quad (2)$$

where μ_d is the dynamic friction coefficient, μ_s is the static friction coefficient, D is the slip and D_c is the slip-weakening distance. A static friction coefficient of 0.6 and a dynamic friction coefficient of 0.35—parameters commonly found in laboratory experiments (e.g. Pec *et al.* 2016) and used in dynamic simulation studies (e.g. Aochi *et al.* 2006; Aochi & Ulrich 2015)—are applied across the fault. As a result, the modeled fault segment is subjected to a stress drop of 4.2 MPa (respectively, 3.8 MPa) for the vertical fault (respectively, south-dipping fault), whereas the strength parameter S is equal to 2.26 (respectively, 2.21) (Das & Aki 1977). The mathematical expression for S is provided by

$$S = \frac{\mu_s \sigma_n - \tau_o}{\tau_o - \mu_d \sigma_n} \quad (3)$$

where τ_o is the initial shear stress, $\mu_s \cdot \sigma_n$ is the failure stress and $\mu_d \cdot \sigma_n$ is the sliding stress. Table 3 summarizes the values of the aforementioned parameters for the dynamic rupture simulations conducted in this study.

Table 3. Model parameters for dynamic rupture simulations.

Model parameter	Value
Static friction coefficient	0.60
Dynamic friction coefficient	0.35
Slip-weakening distance	0.30 m
Element size	250 m
Nucleation radius	2500 m
Time step	0.01 s

Since it is not possible to predict the exact location of the nucleation of rupture for a potential earthquake, we consider two hypothetical locations of the hypocentre along the fault strike (~35 km apart). Both hypocentres lie near the base of the seismogenic zone (~10 km deep). We initiate the rupture by generating a circular crack of 2.5 km radius over a zone where we impose the shear stress to be 5 per cent greater than the failure stress (Day 1982; Madariaga *et al.* 1998). In addition to varying the hypocentre location, we also consider heterogeneity in the initial shear stress. Scenario A contains two patches of 6.5 km radius over which the shear stress is 15 per cent greater than the initial shear stress on the fault. In scenario B, we increase the shear stress by 15 per cent in the upper 5 km of the fault in order to mimic the shear stress increase found along the upper part of the EPGF segment adjacent to the Léogâne Fault resulting from the 2010 Haiti earthquake (Symithe *et al.* 2013; Douilly *et al.* 2015). Due to this complexity in heterogeneity, regions of higher shear stress are subject to an increase in stress drop to 7.7 MPa for a vertical fault and 7.0 MPa for a south-dipping fault, which is still within the typical stress drop range inferred by Hardebeck & Aron (2009). As a result, the strength parameter within those patches of shear stress increase is reduced to 0.76 and 0.79 for a vertical and south-dipping fault, respectively. Although only a few cases have been reported in the literature, a large near-surface stress drop or fault slip can occur during an earthquake (e.g. 1992 Landers, 1999 Hector Mine and 2002 Denali earthquakes) (Wald & Heaton 1994; Bouchon *et al.* 1998; Jónsson *et al.* 2002; Wright

Table 4. Description of low-frequency ground motion simulation scenarios.

			Hypocentre Location		
Scenario	Dip (°)	Stress pattern	Longitude (°)	Latitude (°)	Depth (km)
DA1	65S	Scenario A	−72.591	18.422	10.0
DB1	65S	Scenario B	−72.591	18.422	10.0
VA1	90	Scenario A	−72.584	18.467	10.0
VB1	90	Scenario B	−72.584	18.467	10.0
DA2	65S	Scenario A	−72.337	18.447	10.0
DB2	65S	Scenario B	−72.337	18.447	10.0
VA2	90	Scenario A	−72.350	18.498	10.0
VB2	90	Scenario B	−72.350	18.498	10.0

et al. 2004). In summary, eight scenarios are considered (Table 4) where we vary fault geometry, hypocentre location and initial shear stresses (Fig. 3). For a type A (respectively, type B) scenario where rupture initiates at location 1 (respectively, location 2) on a south-dipping (respectively, vertical) fault, we will refer to it as scenario DA1 (respectively, VB2). We emphasize that the cases considered in this study represent only a subset of all potential rupture scenarios that are compatible with the geological and seismological information available.

4 SYNTHESIS OF HIGH-FREQUENCY GROUND MOTION USING THE SPECIFIC BARRIER MODEL AND THE STOCHASTIC MODELING APPROACH

We generate the high-frequency components of the synthetic ground motion using the specific barrier model (SBM, Papageorgiou & Aki 1983a, b; Papageorgiou 2003) and the stochastic modeling approach (Boore 1983; Shinozuka 1988). The SBM is a particular case of a composite seismic source model according to which the seismic moment is distributed in a deterministic manner on the fault plane on the basis of moment and area constraints. The SBM applies both in the near- and far-field regions, allowing for consistent ground motion simulations over a wide frequency range and for all distances of engineering interest. In the SBM, the fault is visualized as an ensemble of non-overlapping circular subevents (shear cracks) of equal diameter $2\rho_0$ (also known as barrier interval) that cover a rectangular fault with length L and width W (Fig. 4). As the rupture front propagates along the fault, a local stress drop $\Delta\sigma_L$ occurs on each subevent. The subevent rupture starts from its centre and spreads radially outward with a constant spreading velocity υ until it is arrested by the barriers, which are denoted by the shaded area between the subevents in Fig. 4. The SBM has been calibrated to shallow crustal earthquakes of three different tectonic regions (interplate, intraplate and extensional regimes, Halldorsson & Papageorgiou 2005). Given an earthquake magnitude and a tectonic setting, the interdependence of other source parameters on the local stress drop $\Delta\sigma_L$ and the barrier interval $2\rho_0$ allows the causative earthquake fault to be constructed. In a recent study, Halldorsson & Papageorgiou (2012a) relaxed the basic assumption of non-overlapping circular subevents of equal diameter by allowing the subevents to vary in size according to various prescribed probability density functions controlling the frequency of occurrence of subevent sizes.

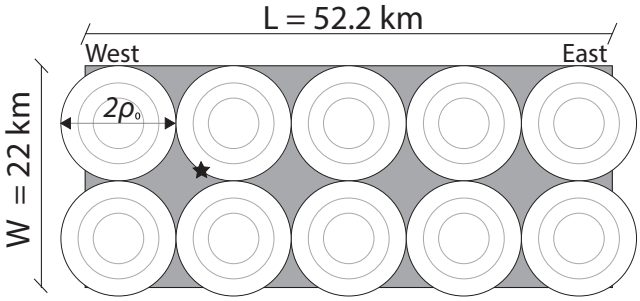

Figure 4. Schematic view of the SBM consisting of equal-size subevents arranged in a non-overlapping manner on the considered fault plane. The black star represents the hypocentre location (i.e. location 1 for scenarios listed in Table 4).

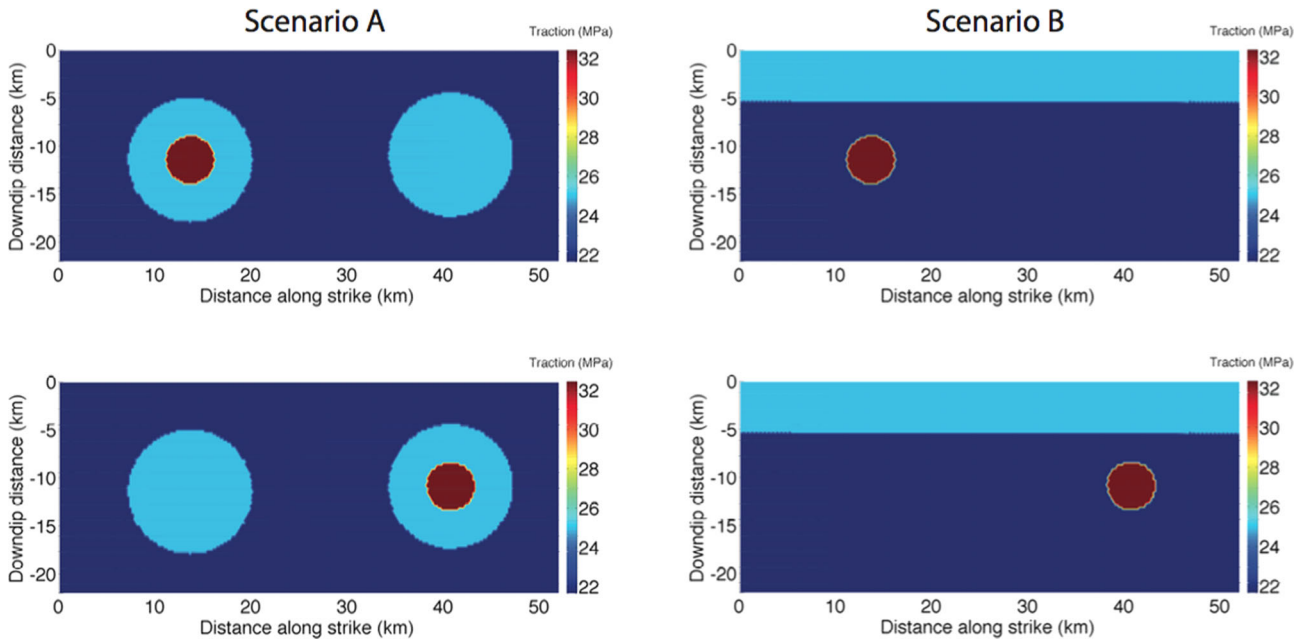

Figure 3. Scenarios of initial shear stress considered in our low-frequency ground motion simulations using dynamic rupture modeling. The red circular asperity—over which the shear stress is greater than the initial shear stress—represents the area where fault rupture initiates. Scenario A: two patches over which the shear stress is 15 per cent greater than the initial shear stress. Scenario B: shear stress is 15 per cent greater than the initial shear stress in the upper 5 km of the fault.

Table 5. Calibration parameters of the SBM for interplate earthquakes (from Halldorsson & Papageorgiou 2005).

Model parameter	Value or function
Global stress drop ($\Delta\sigma_G$)	30E+05 Pa
Local stress drop ($\Delta\sigma_L$)	161E+05 Pa
Shear wave velocity (β)	3.5 km s^{-1}
Material density (ρ)	2800 kg m^{-3}
Free-surface amplification (F)	2
Partition onto two horizontal components (V)	0.71
Averaged radiation pattern for S waves ($R_{\theta\phi}$)	0.55
High-frequency filter (κ)	0.05 s
Distance (r)	$r = (R_{JB}^2 + d^2)^{1/2}$, where: $\ln d = 0.515 + 0.259M_w$
Geometric attenuation	r^{-1} $r \le 30$ km; $(30r)^{-0.5}$ $r > 30$ km
Q attenuation	$Q(f) = 153 f^{0.88}$
Site amplification	Soil: non-linear
Duration (T)	$T = T_S + 0.05r$
High-frequency source complexity factor (ζ)	$\zeta = 10^{2\eta}$, where: $\eta = -0.12(M_w - 6.3)$

The stochastic modeling approach (Boore 1983; Shinozuka 1988) has extensively been used by engineers (using empirical spectra) and seismologists (using spectra derived from physical models of the source). The intent of this approach to strong motion simulation is to capture the essential characteristics of high-frequency motion at an average site from an average earthquake of specified magnitude. Table 5 summarizes the stochastic model and the corresponding parameters that were either selected or obtained in the calibration of the SBM to strong motion data of interplate earthquakes in the context of the stochastic modeling approach (Halldorsson & Papageorgiou 2005). These model parameters are used in this study to simulate the high-frequency components of the synthetic ground motion.

Since all stations of interest are in the near field of the ruptured fault (Fig. 2), it is necessary to simulate time histories for each individual subevent of the SBM, rather than for the entire seismic event as an aggregate of subevents. As explained by Halldórsson *et al.* (2011), the subevent time histories are subsequently summed up at the station, appropriately lagged in time accounting for the time it takes the rupture front to reach the subevent and for the traveltime of the seismic radiation from the subevent to the station. For a particular station, the arrival time of the seismic radiation emitted by each subevent is estimated using the concept of isochrones (Spudich & Frazer 1984; Halldorsson & Papageorgiou 2012b). The isochrones are computed based on the rupture times obtained from the dynamic rupture simulation and the traveltimes obtained using the fault-to-station geometry and the 1-D velocity model in Table 2. The high-frequency time histories simulated in this manner account for the effects that the fault geometry and rupture progression have on the high-frequency strong motion expected at the station.

The calibrated SBM has adopted the National Earthquake Hazards Reduction Program (NEHRP) site classes, based on the average shear wave velocity in the uppermost 30 m (V_{S30}), as indicators of site response (Halldorsson & Papageorgiou 2005). This includes application of the non-linear site amplification function for soil sites proposed by Atkinson & Silva (2000). Recent studies in Haiti have used cross analysis of geological, geotechnical and geophysical data to define the soil classes in Port-au-Prince (Cox *et al.* 2011; Gilles *et al.* 2013). Based on these studies, the soil conditions in Port-au-Prince can predominantly be characterized as Site Class C. It is only the coastal areas and the region north of the city where soil conditions consistent with Site Class D and Site Classes A–B, respectively, are observed. For the 13 stations (APP, HVPR, CIM, HBME, PAP, HVGZ, HPLZ, HVCV, HHMT, CFR, FRE, TDE and HCEA) located in or near Port-au-Prince, we determine the soil type based on the V_{S30} values reported by Gilles *et al.* (2013). For the remaining stations where no V_{S30} values are available, we use a generic Site Class C. The only exception is the station in Léogâne (LEO), where we assign a Site Class D based on findings of a near-surface seismic investigation (Kocel *et al.* 2016). Table 1 summarizes the NEHRP site classification for all stations considered in this study.

Similar to the procedure adopted by Mavroeidis & Scotti (2013), we consider two modeling approaches that involve variable- and uniform-size subevents to generate the high-frequency components of the synthetic ground motion for each of the eight scenarios of dynamic rupture simulation summarized in Table 4. For both modeling approaches, we generate 20 realizations to account for the uncertainty in the amplitude of the white Gaussian noise which is utilized to simulate the high-frequency ground motion.

In the first modeling approach, the fault rupture is represented by an aggregate of N variable-size subevents. The seismic moment $M_{0,i}$ of an individual subevent i represented by a circular crack of radius R_i is provided by eq. (4), whereas the total seismic moment M_0 of the aggregate of all subevents is expressed by eq. (5) (Papageorgiou & Aki 1983a):

$$M_{0,i} = \frac{16}{7}\Delta\sigma_L R_i^3 \tag{4}$$

$$M_0 = \sum_{i=1}^{N} M_{0,i} \tag{5}$$

For the variable-size subevent distributions shown in Figs 5 and 6, the total seismic moment M_0 is obtained from the dynamic rupture simulation, the local stress drop $\Delta\sigma_L$ is set equal to 161E+05 Pa (see Table 5), and the number N and radii R_i of the subevents are determined so as to satisfy eq. (5) and match, to the extent possible, the spatial distribution of slip obtained from the dynamic rupture simulation (see also discussion in Section 5.1). It should be noted that there is no unique way of determining the number, size and location of the variable-size subevents on the fault plane, but the particular characteristics of the subevent distribution are not expected to affect significantly the simulations results. As has been demonstrated by Halldorsson & Papageorgiou (2012a), the differences observed in spectral amplitudes for different subevent distributions are typically

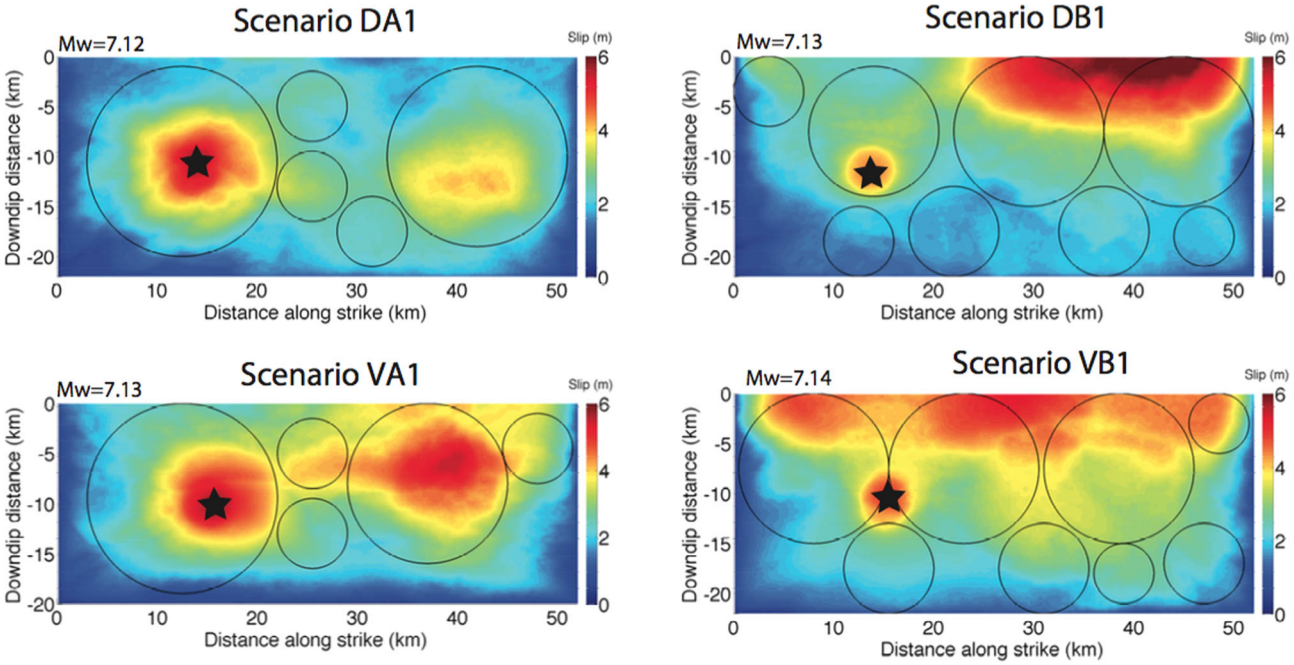

Figure 5. Distributions of final slip for scenarios DA1, DB1, VA1 and VB1 obtained from dynamic simulations based on rupture initiation at location 1. The black star shows the hypocentre location. The black circles represent the distribution of variable-size subevents for the simulation of high-frequency ground motion using the SBM.

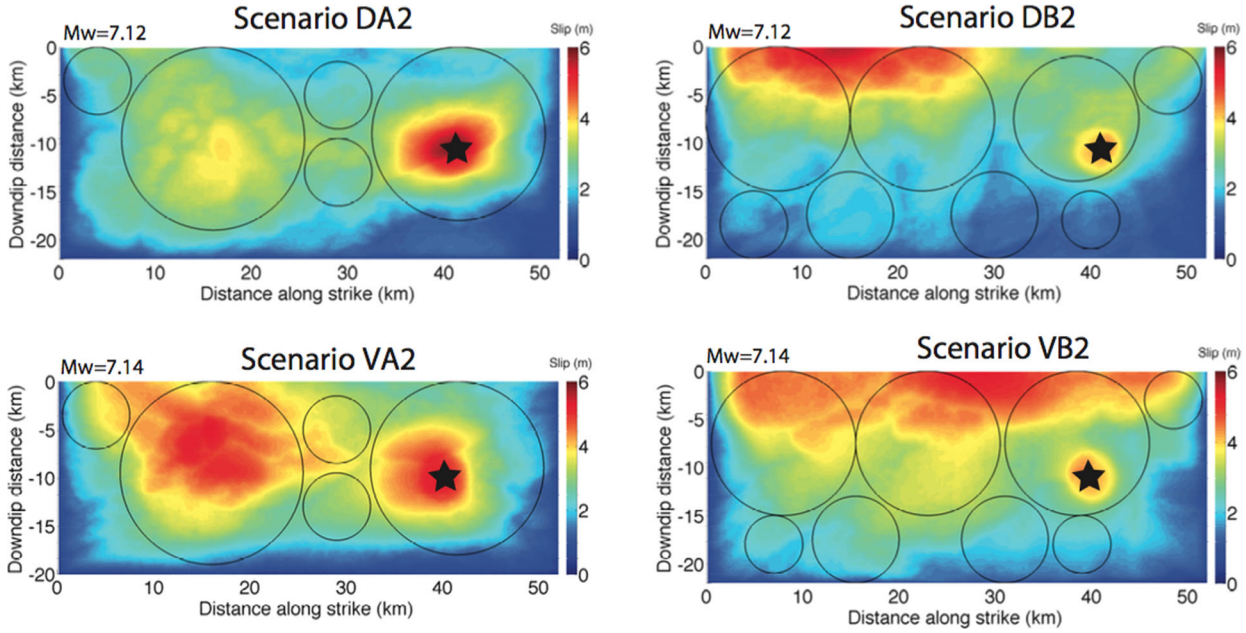

Figure 6. Distributions of final slip for scenarios DA2, DB2, VA2 and VB2 obtained from dynamic simulations based on rupture initiation at location 2. The black star shows the hypocentre location. The black circles represent the distribution of variable-size subevents for the simulation of high-frequency ground motion using the SBM.

less than the expected uncertainty associated with the estimation of the local stress drop from strong motion data.

The average far-field *S*-wave radiation from an individual subevent i is then represented by a source spectrum $S_i(f)$, which can conveniently be approximated by an 'ω-square' spectrum (Aki 1967) with corner frequency $f_{2,i}$ and subevent seismic moment $M_{0,i}$ (Papageorgiou 1988):

$$S_i(f) = \frac{M_{0,i}}{1 + \left(\frac{f}{f_{2,i}}\right)^2} \tag{6}$$

The corner frequency $f_{2,i}$ is related to the radius R_i of the subevent and is given by

$$f_{2,i} = \frac{C_s \beta}{2\pi R_i} \tag{7}$$

where β is the shear wave velocity in the vicinity of the source, C_s is a model-dependent implicit function of υ/β ($1.72 \leq C_s \leq 1.85$ for $0.7 \leq \upsilon/\beta \leq 0.9$) for the symmetric circular crack (Sato & Hirasawa

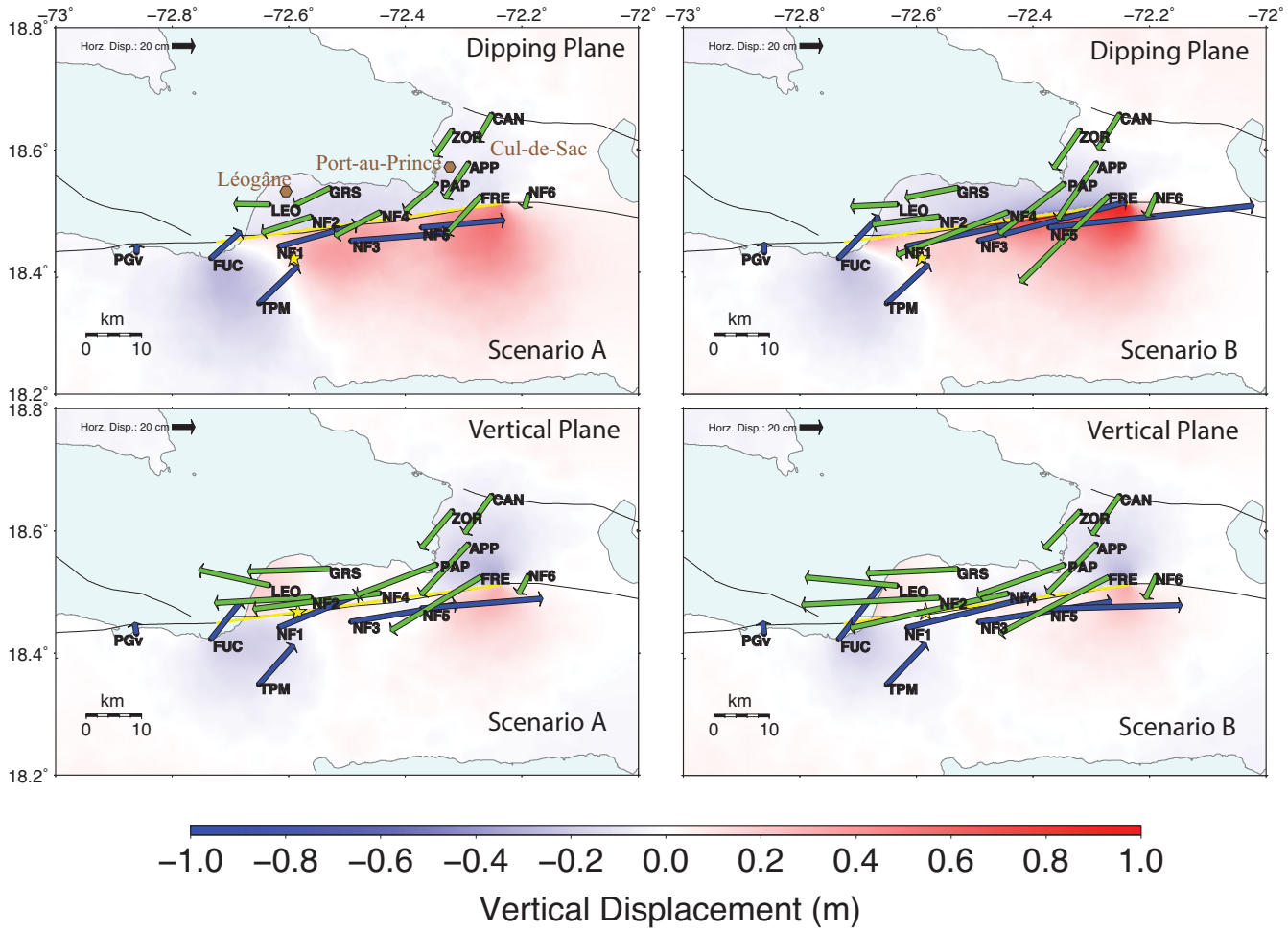

Figure 7. Surface displacements for scenarios DA1, DB1, VA1 and VB1 obtained from dynamic rupture simulations based on hypocentre location 1. The arrows represent the horizontal permanent displacement at selected stations and the colour gradient characterizes the vertical permanent displacement. The yellow star marks the epicentre location and the yellow line shows the ruptured segment.

1973) and υ is the spreading velocity of rupture inside the subevent.

In the second modeling approach, we represent the fault rupture by an aggregate of uniform-size subevents filling up the rectangular fault plane. We consider a fixed number of 10 subevents (Fig. 4) and equally distribute the total seismic moment obtained from the dynamic rupture simulation to them. By combining eqs (4) and (5) and by setting the local stress drop $\Delta\sigma_L$ equal to 161E+05 Pa (see Table 5), we determine the diameter of the subevents (also known as barrier interval) to be 11.4 km.

5 SIMULATION RESULTS

5.1 Low-frequency ground motion

Fig. 5 shows the final distribution of slip on the fault plane for hypocentre location 1 and scenarios A and B, both for the cases of south-dipping and vertical faults (Table 4). For all configurations shown in Fig. 5, the fault rupture initiates near Léogâne at 10 km depth. For scenario A, the rupture delineates two distinct slip patches between depths of 5–15 km, roughly coinciding with the regions over which the shear stress is increased (see Section 3.2 and Fig. 3). For scenario B, slip is predominantly concentrated near the surface consistent with the shear stress increase in the upper 5 km of the fault rupture (see Section 3.2 and Fig. 3). We obtain similar results when the fault rupture initiates near Port-au-Prince at 10 km depth (hypocentre location 2; see Fig. 6). Despite differences in the slip distribution, the cumulative moment release for all cases shown in Figs 5 and 6 results in an $M_w \sim 7.1$, which is within the range of expected magnitude for a fault of this length (Wells & Coppersmith 1994) and consistent with historical earthquakes and fault segmentation in southern Haiti.

Figs 7 (hypocentre at location 1) and 8 (hypocentre at location 2) show the horizontal permanent displacements at selected stations and the spatial distribution of vertical permanent displacements over an extended area for all scenarios of dynamic rupture simulation listed in Table 4. Stations located north of the causative fault experience larger horizontal permanent displacements for a rupture on a vertical fault than for a rupture on a south-dipping fault. For instance, for scenario A in Fig. 7, station LEO has a horizontal permanent displacement of 30 cm (respectively, 50 cm) from rupture on a south-dipping (respectively, vertical) plane. Furthermore, the horizontal permanent displacements at stations PAP, GRS and NF2 are at least 1.5 times greater for the vertical plane than for the south-dipping plane. In addition, even though the seismic moment release for scenarios A and B is approximately the same, the horizontal permanent displacements are typically greater for scenario

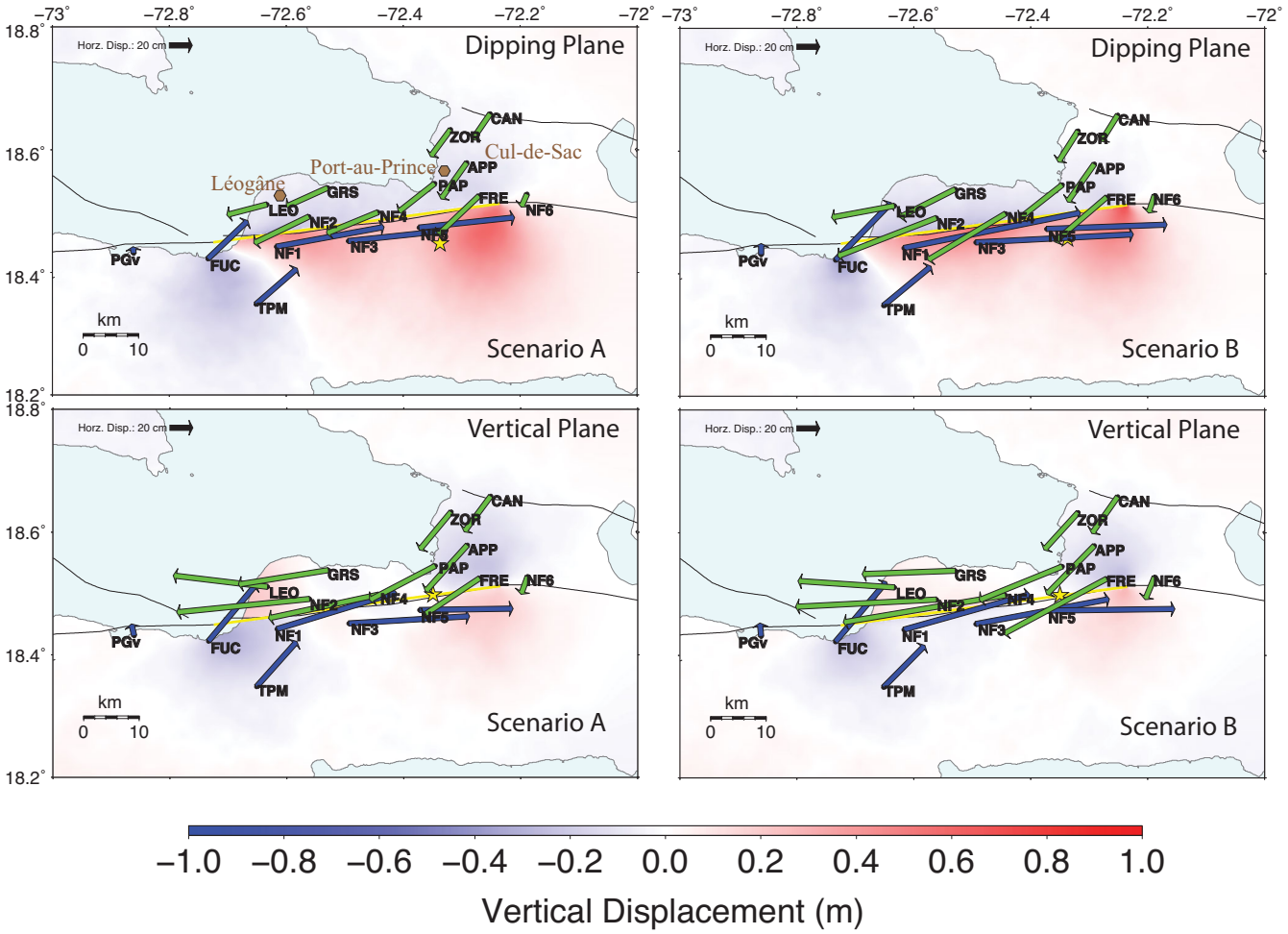

Figure 8. Surface displacements for scenarios DA2, DB2, VA2 and VB2 obtained from dynamic rupture simulations based on hypocentre location 2. The arrows represent the horizontal permanent displacement at selected stations and the colour gradient characterizes the vertical permanent displacement. The yellow star marks the epicentre location and the yellow line shows the ruptured segment.

B than for scenario A. This difference in horizontal permanent displacements is even more pronounced for northern stations located close to the fault. This observation can be attributed to the fact that the slip patches for scenario B are predominantly concentrated near the surface (Figs 5 and 6) and hence generate larger horizontal permanent displacements in the vicinity of the fault. As anticipated, larger vertical permanent displacements are observed for the south-dipping plane than for the vertical plane for both scenarios A and B. Also, in contrast to horizontal permanent displacements, stations located directly south of the ruptured segment (e.g. NF1, NF3 and NF5) experience larger vertical permanent displacements (∼0.8 m uplift) than stations located north of the ruptured segment (e.g. LEO, GRS and PAP) for both scenarios A and B. Therefore, we infer that a vertical (respectively, south-dipping) fault plane generates larger horizontal (respectively, vertical) permanent displacements at stations located north (respectively, south) of the fault.

Despite the fact that the vertical permanent displacements corresponding to hypocentre locations 1 and 2 (Figs 7 and 8) exhibit similar spatial distributions, slight differences can be observed in the respective horizontal permanent displacements. In general, eastern stations (e.g. NF3, NF5, NF6, FRE, PAP and APP) experience larger horizontal permanent displacements for a rupture starting at location 1 than for a rupture starting at location 2. As an example, for scenarios VA1 and VA2, stations NF5 and FRE experience permanent displacements of 100 and 85 cm (respectively, 75 and 60 cm) for a rupture starting at location 1 (respectively, location 2). Similar conclusions can be drawn for western stations (e.g. LEO, GRS and FUC), which experience larger permanent displacements for a rupture starting at location 2 rather than location 1.

Figs 9 and 10 show the spatial distribution of peak ground velocity (PGV) in the fault-normal and fault-parallel directions for the cases of vertical fault rupture. The energy for a rupture initiated at location 1 (respectively, location 2) is more diffused in the easternmost (respectively, westernmost) region. This pattern is more visible for scenario A than for scenario B due to the fact that the slip patches for the former scenario are located at greater depths. The peak horizontal ground velocities shown in Figs 9 and 10 and Figs S1 and S2 in the Supporting Information incorporate the effects of forward rupture directivity and fling step. Forward directivity occurs when the fault rupture propagates toward a site with a rupture velocity that is approximately equal to the shear wave velocity. As a result, most of the energy arrives coherently in a single, intense, relatively long-period pulse at the beginning of the record representing the cumulative effect of almost all the seismic radiation from the fault. Forward directivity manifests itself in the fault-normal direction for both strike-slip and dip-slip faults (Fig. 9 and Fig. S1, Supporting Information). By initiating the rupture on the western part of the fault segment, the rupture propagates from west to east, thus generating

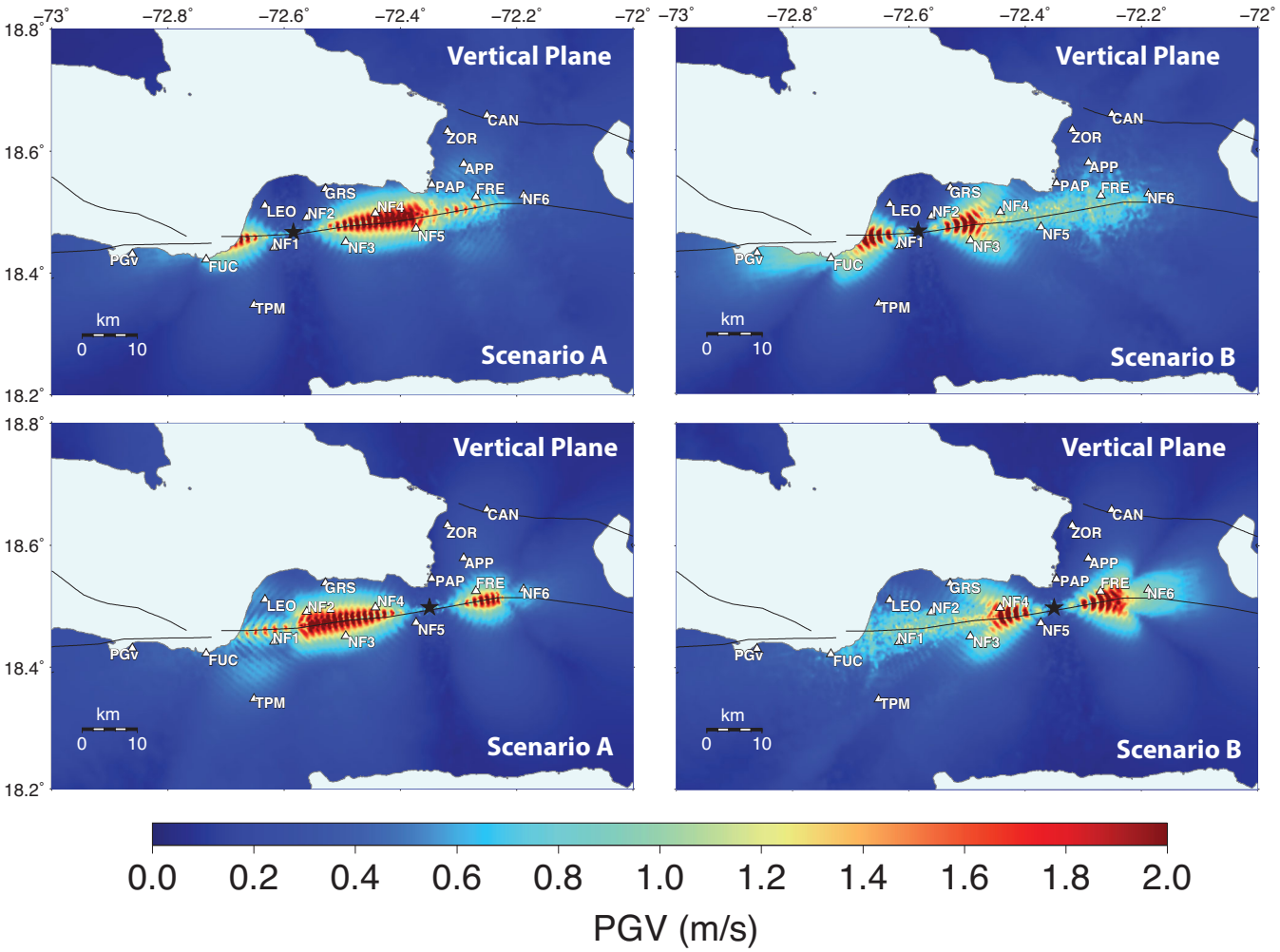

Figure 9. Spatial distribution of peak ground velocity (PGV) in the fault-normal direction obtained from dynamic rupture simulations on a vertical fault. The black star shows the epicentre location, the white triangles mark the location of selected stations and the colour gradient characterizes the magnitude of the peak horizontal ground velocity.

more intense ground velocities near Port-au-Prince than a rupture initiated on the eastern part of the fault segment. On the other hand, fling step is a consequence of permanent fault displacement and appears in the form of one-sided velocity pulse in the fault-parallel direction (Fig. 10 and Fig. S2, Supporting Information). The critical role of rupture directivity and fling step on ground motion has been observed both in ground motion simulations (Aki 1968; Haskell 1969; Mavroeidis & Papageorgiou 2010; Lozos *et al*. 2015) and in numerous actual earthquakes (Somerville *et al*. 1997; Mavroeidis & Papageorgiou 2003; Bray & Rodriguez-Marek 2004).

Certain scenarios, such as DA1 and DA2 or VB1 and VB2, exhibit strong similarities in terms of their distributions of final slip (Figs 5 and 6) and their spatial distributions of permanent ground displacement (Figs 7 and 8). Therefore, to avoid redundancy, we choose to consider only scenarios DA1, VA1, DB1, VB2, VA2 and DB2 in the broad-band ground motion simulations discussed in Section 5.2.

5.2 Broad-band ground motion

We generate three-component time histories of broad-band ground motion for all stations listed in Table 1. To obtain the broad-band synthetics, we combine the low-frequency ground motions from the dynamic rupture simulations (scenarios DA1, VA1, DB1, VB2, VA2 and DB2) with the high-frequency ground motions from the stochastic simulations (uniform- and variable-size subevent distributions) using matched filtering at a crossover frequency of 1 Hz. Figs 11 and 12 present broad-band results of acceleration, velocity and displacement time histories at selected stations (FUC, LEO, NF3, PAP, NF5 and NF4) distributed evenly along the ruptured fault segment, both for the uniform- and variable-size subevent distributions of scenario VA1. The directions pointing north, east and upward define the positive sign convention of the synthetic time histories.

Tables S1 and S2 in the Supporting Information contain the mean and standard deviation values of broad-band PGA for all stations listed in Table 1, obtained by combining simulation results of low- (scenarios DA1, VA1, DB1, VB2, VA2 and DB2) and high-frequency (20 realizations of uniform- and variable-size subevent distributions) synthetics. Figs 13 and 14 illustrate the attenuation of the average horizontal PGA with distance based on broad-band simulation results (uniform- and variable-size subevent distributions) for scenarios DB1, DB2, VA1 and VA2. The circle, square and triangle symbols represent PGA values for NEHRP Site Classes C, D and A–B, respectively. The solid lines indicate the mean curves of the Ground Motion Prediction Equation (GMPE)

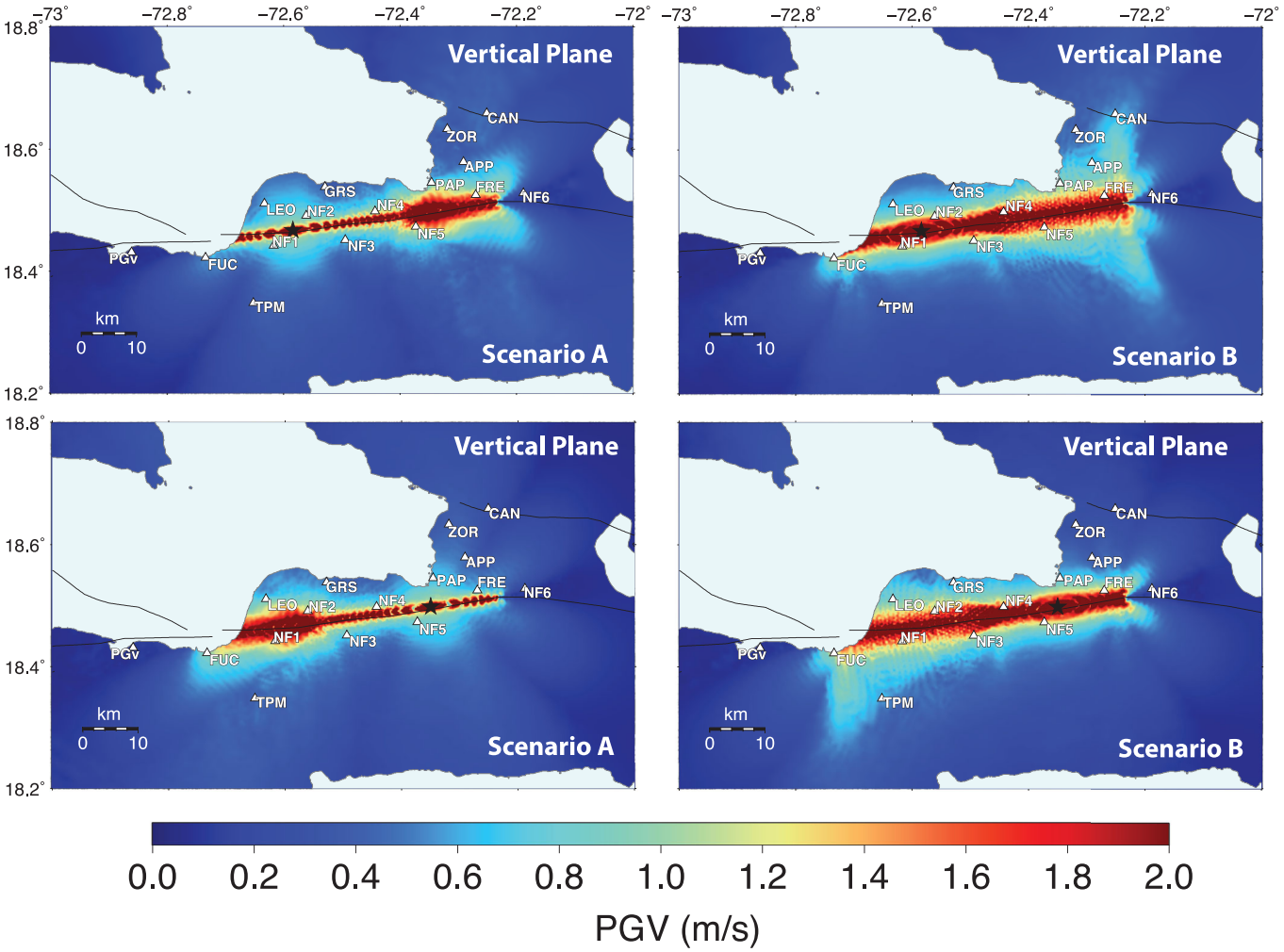

Figure 10. Spatial distribution of peak ground velocity (PGV) in the fault-parallel direction obtained from dynamic rupture simulations on a vertical fault. The black star shows the epicentre location, the white triangles mark the location of selected stations and the colour gradient characterizes the magnitude of the peak horizontal ground velocity.

proposed by Boore & Atkinson (2008) for the average horizontal PGA, whereas the dashed lines represent plus or minus one standard deviation around the mean. The GMPE curves have been plotted for NEHRP Site Class C (V_{S30} = 520 m s^{-1}) consistent with the site conditions of the majority of stations considered in our simulations. Data points with Joyner–Boore distance less than 0.1 km are plotted at 0.1 km. Figs 13 and 14 indicate that the synthetic PGA values are in good agreement with the GMPE proposed by Boore & Atkinson (2008), with most Site Class C stations lying between the mean and mean minus one standard deviation curves. As anticipated, Site Class D stations have on average greater PGA values than Site Class C stations. Station PAP has a mean horizontal PGA of ∼0.45 g (respectively, ∼0.35 g) for a rupture on a vertical (respectively, south-dipping) fault for the uniform and variable-size subevent distributions, whereas the maximum horizontal PGA among all realizations is ∼0.60 g. Nevertheless, it should be pointed out that the range of response defined by our realizations does not represent the entire uncertainty that characterizes the problem under investigation (see discussion in Mavroeidis & Scotti 2013).

Similar to the low-frequency simulation results presented in Section 5.1, stations located north of the ruptured fault segment experience higher PGA for a vertical fault (scenario VA1) than for a south-dipping fault (scenario DA1) due to the shorter distance of these stations to the vertical fault plane. In addition, for the uniform-size subevent distribution, PGA values at stations near Port-au-Prince are approximately the same for ruptures initiated at hypocentre locations 1 and 2 (scenarios VA1 versus VA2 and scenarios DB1 versus DB2) (Fig. 13 and Table S1, Supporting Information). However, this is not the case for the variable-size subevent distribution (Fig. 14 and Table S2, Supporting Information). Rupture at hypocentre location 2 generates higher PGA values for stations in Port-au-Prince than rupture at hypocentre location 1 (scenarios VA2 versus VA1 and scenarios DB2 versus DB1). For instance, stations HBME, APP, HVPR and PAP have a mean horizontal PGA of ∼0.26, ∼0.26, ∼0.32 and ∼0.44 g for scenario VA1 and ∼0.38, ∼0.33, 0.42 and ∼0.57 g for scenario VA2 (Table S2, Supporting Information). This difference in results between hypocentre locations 1 and 2 for the variable-size subevent distribution is primarily attributed to the location and size of the subevents in the proximity of Port-au-Prince rather than the location of the hypocentre itself.

6 DISCUSSION

Despite the fact that no strong motion instruments were operating in the source region at the time of the 2010 Haiti earthquake, several studies have attempted to estimate the ground shaking level mostly

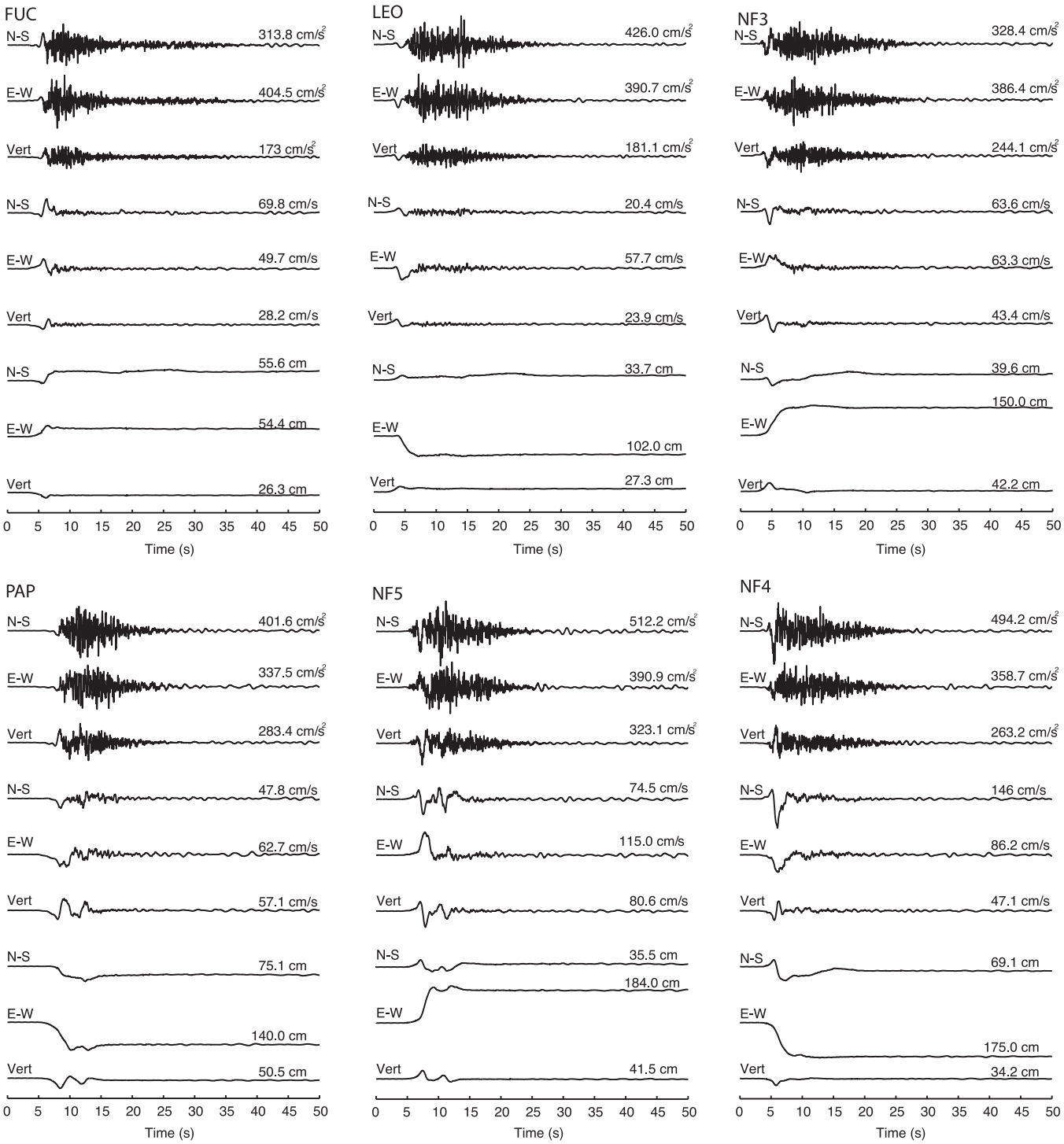

Figure 11. Broad-band acceleration, velocity and displacement time histories at selected stations obtained by combining low- (scenario VA1) and high-frequency (uniform-size subevent distribution) simulation results.

in the Port-au-Prince urban area. Low-frequency dynamic rupture simulations conducted by Douilly *et al*. (2015) on the Léogâne Fault predicted the PGA in Port-au-Prince to be ∼0.1 g. This PGA estimate is low compared to other studies because dynamic rupture simulations with simplistic stress complexity and based on 1-D velocity models do not account for higher frequencies that are necessary to adequately resolve the PGA at a site. Dynamic rupture studies have shown that complexities, such as fault roughness or stochastic stress asperities, can lead a rupture to reach higher frequencies (Oglesby & Day 2002; Shi & Day 2013, Lozos *et al*. 2015). Furthermore, Hough *et al*. (2012) used a rigid body displacement technique and inferred a PGA value of ∼0.2 g in Port-au-Prince, not too far off from that of Douilly *et al*. (2015). The U.S. Geological Survey ShakeMap and Olson *et al*. (2011) estimated the PGA in Port-au-Prince to be of the order of 0.3 g. Goodno *et al*. (2011) correlated average structural damage at specific sites to estimated ground motion from other studies to infer a mean PGA in Port-au-Prince of the order of 0.13–0.47 g. Finally, Mavroeidis & Scotti (2013)

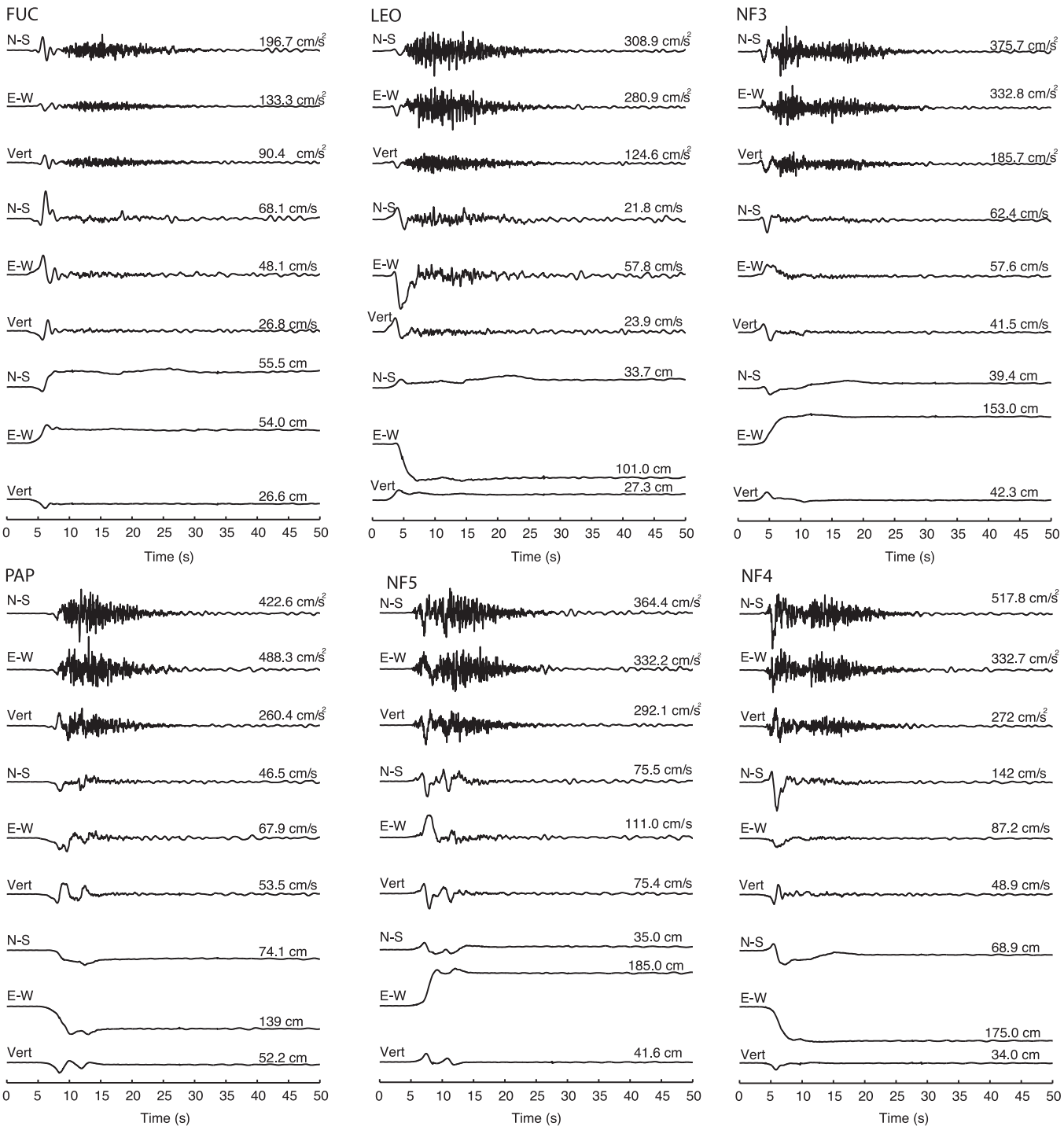

Figure 12. Broad-band acceleration, velocity and displacement time histories at selected stations obtained by combining low- (scenario VA1) and high-frequency (variable-size subevent distribution) simulation results.

used the coseismic slip distribution from Hayes *et al*. (2010) to simulate broad-band ground motions by combining low-frequency synthetics generated using the discrete wavenumber representation method (Bouchon 1979) with high-frequency synthetics generated using the SBM (Papageorgiou & Aki 1983a,b; Papageorgiou 2003). They estimated the mean PGA in Port-au-Prince to be 0.20–0.33 g.

Our broad-band simulations for a rupture on a vertical (respectively, south-dipping) EPGF indicate that the mean PGA in Port-au-Prince is ∼0.45 g (respectively, 0.35 g), which is about 1.5–2.0 times greater than the estimated PGA from the 2010 Haiti earthquake on the Léogâne Fault, whereas the maximum PGA could reach values up to ∼0.6 g. However, it should be pointed out that other potential fault segments, closer to Port-au-Prince, could generate even more intense ground motions in this area. For instance, Symithe & Calais (2016) used a crude ground ShakeMap-type calculation to show that ground shaking from a rupture on a

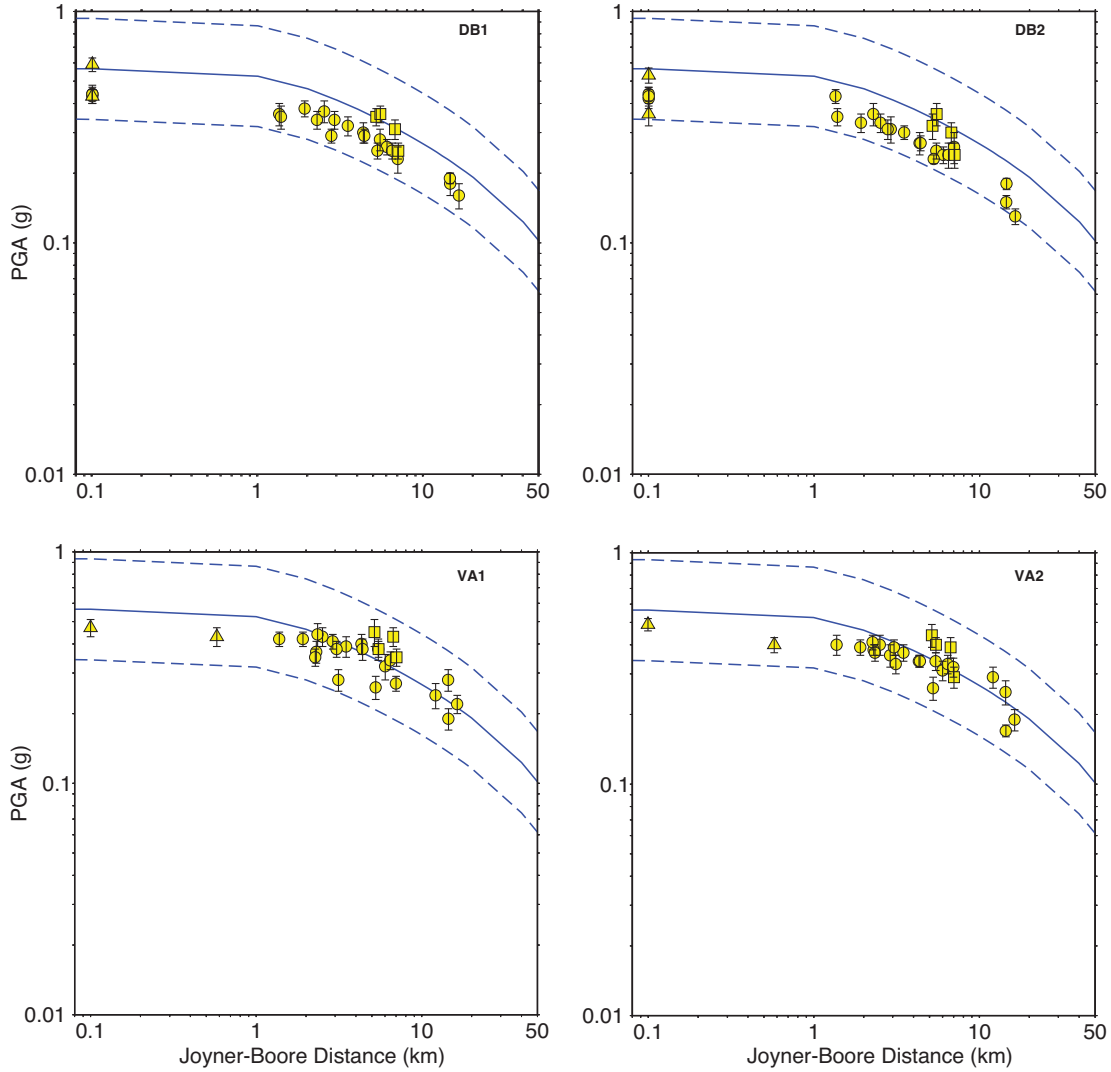

Figure 13. Comparison of average horizontal PGA obtained from broad-band simulations (uniform-size subevent distribution) for scenarios DB1, DB2, VA1 and VA2 with the GMPE (NEHRP Site Class C) proposed by Boore & Atkinson (2008). The solid blue lines indicate the mean curves of the GMPE, whereas the dashed blue lines represent plus or minus one standard deviation around the mean. The circle, square and triangle symbols represent PGA values from our simulations for NEHRP Site Classes C, D and A–B, respectively. The vertical black lines within the symbols represent the standard deviation of each data point. Data points with Joyner–Boore distance less than 0.1 km are plotted at 0.1 km.

shallow south-dipping reverse fault segment along the southern edge of the Cul-de-Sac Basin may generate a PGA up to ∼0.75 g in Port-au-Prince.

We note that our simulations should be considered as the lower bound of the ground motion variability spectrum since other localized effects, besides soil type, not taken into account in this study, could amplify ground shaking. Hough *et al*. (2010) investigated ground motion throughout Port-au-Prince from smaller events following the 2010 Haiti earthquake and found that topographic amplification could explain some of the localized damage observed. In a recent study, St Fleur *et al*. (2016) used aftershock data from the 2010 Haiti earthquake along with spectral ratio methodologies and 1-D simulation analysis in soil columns to estimate ground motion amplification at seismological stations deployed in Port-au-Prince after the event. At most of the stations (HPKH, HBME, USEM, HPLZ, HVGZ and HHMT), the amplification at low frequencies was found to be slightly lower than 3. However, strong amplification was observed at two stations (HVCV and HVPR) in the 1–5 Hz frequency range, which was attributed to lithological and topographic site effects. Station HVPR (with amplification greater than 5) is located less than 5 km away from station PAP considered in our analysis, with the same soil type. Therefore, it is not unreasonable to assume that station PAP could experience similar amplification as station HVPR, thus increasing the intensity of the synthetic ground motion over the particular frequency range.

7 CONCLUSIONS

We generated broad-band ground motions in the vicinity of a hypothetical M_w 7.1 earthquake consistent with a 52-km-long rupture on the plate boundary fault segment adjacent to, and to the east of, the 2010 Léogâne Fault rupture in Haiti. Field observations have shown evidence of recent earthquake ruptures (Prentice *et al*. 2010) and geodetic measurements have attested that this fault segment is currently accumulating elastic strain likely to be released

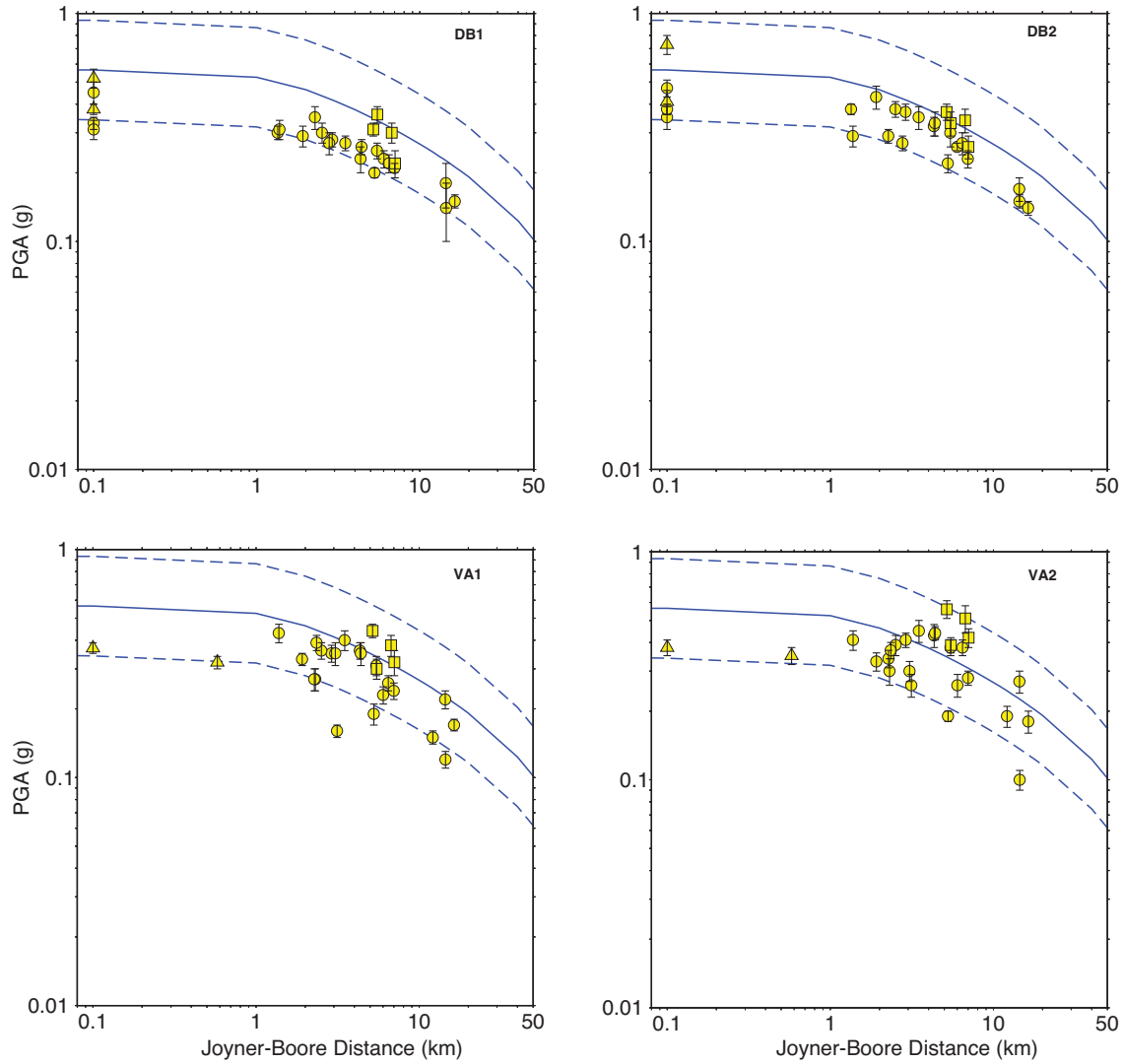

Figure 14. Comparison of average horizontal PGA obtained from broad-band simulations (variable-size subevent distribution) for scenarios DB1, DB2, VA1 and VA2 with the GMPE (NEHRP Site Class C) proposed by Boore & Atkinson (2008). The solid blue lines indicate the mean curves of the GMPE, whereas the dashed blue lines represent plus or minus one standard deviation around the mean. The circle, square and triangle symbols represent PGA values from our simulations for NEHRP Site Classes C, D and A–B, respectively. The vertical black lines within the symbols represent the standard deviation of each data point. Data points with Joyner–Boore distance less than 0.1 km are plotted at 0.1 km.

in future earthquakes (Calais *et al*. 2010). In addition, Symithe *et al*. (2013) showed that coseismic Coulomb failure stress changes caused by the 2010 earthquake have likely brought this segment closer to rupture. We used dynamic rupture simulations to generate the low-frequency ground motion and the SBM (in the context of the stochastic modeling approach) to generate the high-frequency ground motion. The two independently derived ground motion components were then combined using matched filtering at a crossover frequency of 1 Hz to generate broad-band ground motions consistent with eight scenarios representing plausible fault dips, hypocentre locations and initial shear stresses. Despite the limited number of scenarios, results from the low-frequency simulations showed that a vertical EPGF generates larger horizontal permanent displacements for stations located north of the fault segment than a south-dipping EPGF. Broad-band ground motion simulations showed that the mean PGA in Port-au-Prince is ∼0.45 g, which is about twice as much as the estimated PGA during the 2010 Haiti earthquake. The fact that the intensity of ground motion experienced in Port-au-Prince during the 2010 earthquake could be surpassed during the rupture of the fault segment modeled in this study should serve as a warning for Haitian engineers and the population in general. The 2010 earthquake, as devastating as it was to Port-au-Prince, is unfortunately not the worst-case scenario for the region. Given that the fault rupture simulated here—consistent with geological and geodetic evidences—could be even more disastrous than the 2010 Haiti earthquake, stringent measures must be taking place in order to reinforce buildings, particularly critical facilities (hospitals, civil protection centres) and high-occupancy buildings (schools and public administrations), at least to the standards described in the recently published Haiti Building Code (CNBH 2012).

ACKNOWLEDGEMENTS

This research was supported by a COCONet Graduate Fellowship from UNAVCO to RD and by the U.S. National Science Foundation award EAR-1045809 to EC. The figures were

generated using GMT (Wessel & Smith 1998) and MATLAB (available at: http://www.mathworks.com/products/matlab/). We thank Didier Bertil and Sadrac St Fleur for helpful discussions and two anonymous reviewers for their constructive comments that led to improvements in the manuscript.

REFERENCES

Aagaard, B., Knepley, M. & Williams, C., 2013. A domain decomposition approach to implementing fault slip in finite-element models of quasi-static and dynamic crustal deformation, *J. geophys. Res.,* **118,** 1–21.

Aagaard, B.T., Anderson, G. & Hudnut, K.W., 2004. Dynamic rupture modeling of the transition from thrust to strike-slip motion in the 2002 Denali fault earthquake, Alaska, *Bull. seism. Soc. Am.,* **94,** S190–S201.

Aki, H., 1967. Scaling law of seismic spectrum, *J. geophys. Res.,* **72,** 1217–1231.

Aki, H., 1968. Seismic displacement near a fault, *J. geophys. Res.,* **73,** 5359–5376.

Ali, T.S., Freed, A.M., Calais, E., Manaker, D.M. & McCann, W.R., 2008. Coulomb stress evolution in Northeastern Caribbean over the past 250 years due to coseismic, postseismic and interseismic deformation, *Geophys. J. Int.,* **174,** 904–918.

Andrews, D., 1976. Rupture velocity of plane strain shear cracks, *J. geophys. Res.,* **81,** 5679–5687.

Angelier, J., 1979. Determination of the mean principal directions of stresses for a given fault population, *Tectonophysics,* **56,** T17–T26.

Angelier, J., 1990. Inversion of field data in fault tectonics to obtain the regional stress—III. A new rapid direct inversion method by analytical means, *Geophys. J. Int.,* **103,** 363–376.

Aochi, H. & Ulrich, T., 2015. A probable earthquake scenario near Istanbul determined from dynamic simulations, *Bull. seism. Soc. Am.,* **105,** 1468–1475.

Aochi, H., Cushing, M., Scotti, O. & Berge-Thierry, C., 2006. Estimating rupture scenario likelihood based on dynamic rupture simulations: the example of the segmented Middle Durance fault, southeastern France, *Geophys. J. Int.,* **165,** 436–446.

Atkinson, G.M. & Silva, W., 2000. Stochastic modeling of California ground motions, *Bull. seism. Soc. Am.,* **90,** 255–274.

Bakun, W.H., Flores, C.H. & Uri, S., 2012. Significant earthquakes on the Enriquillo fault system, Hispaniola, 1500–2010: implications for seismic hazard, *Bull. seism. Soc. Am.,* **102,** 18–30.

Boore, D.M., 1983. Stochastic simulation of high-frequency ground motions based on seismological models of the radiated spectra, *Bull. seism. Soc. Am.,* **73,** 1865–1894.

Boore, D.M. & Atkinson, G.M., 2008. Ground-motion prediction equations for the average horizontal component of PGA, PGV, and 5%-damped PSA at spectral periods between 0.01 and 10.0 s, *Earthq. Spectra,* **24**(1), 99–138.

Bouchon, M., 1979. Discrete wave number representation of elastic wave fields in three-space dimensions, *J. geophys. Res.,* **84,** 3609–3614.

Bouchon, M., Campillo, M. & Cotton, F., 1998. Stress field associated with the rupture of the 1992 Landers, California, earthquake and its implications concerning the fault strength at the onset of the earthquake, *J. geophys. Res.,* **103**(B9), 21 091–21 097.

Bourgueil, B., Andreieff, P., Lasnier, J., Gonnard, R., Le Metour, J. & Rancon, J.P., 1988. Synthèse géologique de la République d'Haïti. Technical Rep., Bureau des Mines et de L'Energie. Haiti, Port-au-Prince.

Bray, J.D. & Rodriguez-Marek, A., 2004. Characterization of forward-directivity ground motions in the near-fault region, *Soil Dyn. Earthq. Eng.,* **24,** 815–828.

Calais, E. *et al.*, 2010. Transpressional rupture of an unmapped fault during the 2010 Haiti earthquake, *Nat. Geosci.,* **3,** 794–799.

Calais, É., Symithe, S., Mercier de Lépinay, B. & Prépetit, C., 2016. Plate boundary segmentation in the northeastern Caribbean from geodetic measurements and Neogene geological observations, *C. R. Geosci.,* **348,** 42–51.

Calmus, T., 1983. Contribution à l'étude géologique du massif de Macaya (sud-ouest d'Haïti, Grandes Antilles), sa place dans l'evolution de l'orogène nord-caraïbe, *PhD thesis*, Université Pierre Marie, Paris, France.

Code National du Bâtiment d'Haïti (CNBH), 2012. *Ministère des Travaux Publics, Transports et Communications (MTPTC),* République d'Haïti.

Cox, B.R., Bachhuber, J., Rathje, E., Wood, C.M., Dulberg, R., Kottke, A., Green, R.A. & Olson, S.M., 2011. Shear wave velocity- and geology-based seismic microzonation of Port-au-Prince, Haiti, *Earthq. Spectra,* **27,** S67–S92.

Das, S. & Aki, K., 1977. A numerical study of two-dimensional spontaneous rupture propagation, *Geophys. J. R. astr. Soc.,* **50,** 643–668.

Day, S.M., 1982. Three-dimensional simulation of spontaneous rupture: the effect of nonuniform prestress, *Bull. seism. Soc. Am.,* **72,** 1881–1902.

DeMets, C., Jansma, P.E., Mattioli, G.S., Dixon, T.H., Farina, F., Bilham, R., Calais, E. & Mann, P., 2000. GPS geodetic constraints on Caribbean-North America plate motion, *Geophys. Res. Lett.,* **27,** 437–440.

Douilly, R. *et al.*, 2013. Crustal structure and fault geometry of the 2010 Haiti Earthquake from temporary seismometer deployments, *Bull. seism. Soc. Am.,* **103,** 2305–2325.

Douilly, R., Aochi, H., Calais, E. & Freed, A., 2015. Three-dimensional dynamic rupture simulations across interacting faults: the M_w 7. 0, 2010, Haiti earthquake, *J. geophys. Res.,* **120,** 1108–1128.

Gephart, J.W. & Forsyth, D.W., 1984. An improved method for determining the regional stress tensor using earthquake focal mechanism data: application to the San Fernando earthquake sequence, *J. geophys. Res.,* **89,** 9305–9320.

Gilles, R., Bertil, D., Belvaux, M., Roulle, A., Noury, G., Prepetit, C. & Jean-Philippe, J., 2013. Seismic microzoning in the metropolitan area of Port-au-Prince-complexity of the subsoil, in *AGU Fall Meeting Abstracts,* p. 2312, San Francisco, CA.

Goodno, B., Gould, N., Caldwell, P. & Gould, P., 2011. Effects of the January 2010 Haitian earthquake on selected electrical equipment, *Earthq. Spectra,* **27,** S251–S276.

Goulet, C.A., Abrahamson, N.A., Somerville, P.G. & Wooddell, K.E., 2015. The SCEC broadband platform validation exercise: methodology for code, *Seismol. Res. Lett.,* **86**(1), doi:10.1785/0220140104.

Graves, R.W. & Pitarka, A., 2010. Broadband ground-motion simulation using a hybrid approach, *Bull. seism. Soc. Am.,* **100**(5A), 2095–2123.

Halldorsson, B. & Papageorgiou, A.S., 2005. Calibration of the specific barrier model to earthquakes of different tectonic regions, *Bull. seism. Soc. Am.,* **95,** 1276–1300.

Halldorsson, B. & Papageorgiou, A.S., 2012a. Variations of the specific barrier model—Part I: effect of subevent size distributions, *Bull. Earthq. Eng.,* **10,** 1299–1319.

Halldorsson, B. & Papageorgiou, A.S., 2012b. Variations of the specific barrier model—part II: effect of isochron distributions, *Bull. Earthq. Eng.,* **10,** 1321–1337.

Halldórsson, B., Mavroeidis, G.P. & Papageorgiou, A.S., 2011. Near-fault and far-field strong ground-motion simulation for earthquake engineering applications using the specific barrier model, *J. Struct. Eng.,* **137,** 433–444.

Hardebeck, J.L. & Aron, A., 2009. Earthquake stress drops and inferred fault strength on the Hayward fault, east San Francisco Bay, California, *Bull. seism. Soc. Am.,* **99**(3), 1801–1814.

Haskell, N.A., 1969. Elastic displacements in the near-field of a propagating fault, *Bull. seism. Soc. Am.,* **59,** 865–908.

Hauksson, E., Jones, L.M., Hutton, K. & Eberhart-Phillips, D., 1993. The 1992 Landers earthquake sequence: seismological observations, *J. geophys. Res.,* **98,** 19 835–19 858.

Hayes, G. *et al.*, 2010. Complex rupture during the 12 January 2010 Haiti earthquake, *Nat. Geosci.,* **3,** 800–805.

Hough, S.E. *et al.*, 2010. Localized damage caused by topographic amplification during the 2010 M 7.0 Haiti earthquake, *Nat. Geosci.,* **3,** 778–782.

Hough, S.E., Taniguchi, T. & Altidor, J.-R., 2012. Estimation of peak ground acceleration from horizontal rigid body displacement: a case study in Port-au-Prince, Haiti, *Bull. seism. Soc. Am.,* **102,** 2704–2713.

Ida, Y., 1972. Cohesive force across the tip of a longitudinal-shear crack and Griffith's specific surface energy, *J. geophys. Res.,* **77,** 3796–3805.

Jónsson, S., Zebker, H., Segall, P. & Amelung, F., 2002. Fault slip distribution of the 1999 M_w 7.1 Hector Mine, California, earthquake, estimated from satellite radar and GPS measurements, *Bull. seism. Soc. Am.,* **92**(4), 1377–1389.

King, G.C.P., Hubert-Ferrari, A., Nalbant, S.S., Meyer, B., Armijo, R. & Bowman, D., 2001. Coulomb interactions and the 17 August 1999 Izmit, Turkey earthquake, *C. R. Acad. Sci.—Ser. IIA—Earth planet. Sci.,* **333,** 557–569.

Kocel, E., Stewart, R.R., Mann, P. & Chang, L., 2016. Near-surface geophysical investigation of the 2010 Haiti earthquake epicentral area: Léogâne, Haiti, *Interpretation,* **4,** T49–T61.

Lozos, J.C., Olsen, K.B., Brune, J.N., Takedatsu, R., Brune, R.J. & Oglesby, D.D., 2015. Broadband ground motions from dynamic models of rupture on the northern San Jacinto fault, and comparison with precariously balanced rocks, *Bull. seism. Soc. Am.,* **105,** 1947–1960.

Madariaga, R., Olsen, K. & Archuleta, R., 1998. Modeling dynamic rupture in a 3D earthquake fault model, *Bull. seism. Soc. Am.,* **88,** 1182–1197.

Mai, P.M., Imperatori, W. & Olsen, K.B., 2010. Hybrid broadband ground-motion simulations: combining long-period deterministic synthetics with high-frequency multiple S-to-S backscattering, *Bull. seism. Soc. Am.,* **100,** 2124–2142.

Manaker, D.M. *et al.*, 2008. Interseismic plate coupling and strain partitioning in the northeastern Caribbean, *Geophys. J. Int.,* **174,** 889–903.

Mann, P. & Gordon, M.B., 1996. Tectonic uplift and exhumation of Blueschist Belts along transpressional strike-slip fault zones, in *Subduction Top to Bottom*, pp. 143–154, eds Bebout, G.E., Scholl, D.W., Kirby, S.H. & Platt, J.P. American Geophysical Union.

Mann, P., Draper, G. & Lewis, J.F., 1991. Geologic and tectonic development of the North America-Caribbean plate boundary in Hispaniola, *Spec. Pap. Geol. Soc. Am.,* **262,** 1–28.

Mann, P., Taylor, F.W., Edwards, R.L. & Ku, T.-L., 1995. Actively evolving microplate formation by oblique collision and sideways motion along strike-slip faults: an example from the northeastern Caribbean plate margin, *Tectonophysics,* **246,** 1–69.

Mavroeidis, G.P. & Papageorgiou, A.S., 2003. A mathematical representation of near-fault ground motions, *Bull. seism. Soc. Am.,* **93,** 1099–1131.

Mavroeidis, G.P. & Papageorgiou, A.S., 2010. Effect of fault rupture characteristics on near-fault strong ground motions, *Bull. seism. Soc. Am.,* **100,** 37–58.

Mavroeidis, G.P. & Scotti, C.M., 2013. Finite-fault simulation of broadband strong ground motion from the 2010 M_w 7.0 Haiti Earthquake, *Bull. seism. Soc. Am.,* **103,** 2557–2576.

Mavroeidis, G.P., Zhang, B., Dong, G., Papageorgiou, A.S., Dutta, U. & Biswas, N.N., 2008. Estimation of strong ground motion from the great 1964 M_w 9.2 Prince William Sound, Alaska, Earthquake, *Bull. seism. Soc. Am.,* **98,** 2303–2324.

Meng, L., Ampuero, J.-P., Sladen, A. & Rendon, H., 2012. High-resolution backprojection at regional distance: application to the Haiti *M*7. 0 earthquake and comparisons with finite source studies, *J. geophys. Res.,* **117,** B04313, doi:10.1029/2011JB008702.

Mercier de Lépinay, B., *et al.*, 2011. The 2010 Haiti earthquake: a complex fault pattern constrained by seismologic and tectonic observations, *Geophys. Res. Lett.,* **38,** L22305, doi:10.1029/2011GL049799.

Momplaisir, R.B.-A., 1986. Contribution a l'Etude Geologique de la partie orientale du massif de la hotte (presqu'ile de sud d'Haiti): synthese structurale des marges de la presqu'ile a partir de donnees sismiques, *PhD thesis*, Univ. Pierre-et-Marie-Curie (Paris VI), Paris, 210 pp.

Oglesby, D.D. & Day, S.M., 2002. Stochastic fault stress: implications for fault dynamics and ground motion, *Bull. seism. Soc. Am.,* **92**(8), 3006–3021.

Olson, S.M., Green, R.A., Lasley, S., Martin, N., Cox, B.R., Rathje, E., Bachhuber, J. & French, J., 2011. Documenting liquefaction and lateral spreading triggered by the 12 January 2010 Haiti earthquake, *Earthq. Spectra,* **27,** S93–S116.

Papageorgiou, A.S., 1988. On two characteristic frequencies of acceleration spectra: patch corner frequency and fmax, *Bull. seism. Soc. Am.,* **78,** 509–529.

Papageorgiou, A.S., 2003. The barrier model and strong ground motion, *Pure appl. Geophys.,* **160,** 603–634.

Papageorgiou, A.S. & Aki, K., 1983a. A specific barrier model for the quantitative description of inhomogeneous faulting and the prediction of strong ground motion. I. Description of the model, *Bull. seism. Soc. Am.,* **73,** 693–722.

Papageorgiou, A.S. & Aki, K., 1983b. A specific barrier model for the quantitative description of inhomogeneous faulting and the prediction of strong ground motion. Part II. Applications of the model, *Bull. seism. Soc. Am.,* **73,** 953–978.

Pec, M., Stünitz, H., Heilbronner, R. & Drury, M., 2016. Semi-brittle flow of granitoid fault rocks in experiments, *J. geophys. Res.,* **121,** 1677–1705.

Prentice, C., Mann, P., Crone, A., Gold, R., Hudnut, K., Briggs, R., Koehler, R. & Jean, P., 2010. Seismic hazard of the Enriquillo-Plantain Garden fault in Haiti inferred from palaeoseismology, *Nat. Geosci.,* **3,** 789–793.

Saint Fleur, N., Feuillet, N., Grandin, R., Jacques, E., Weil-Accardo, J. & Klinger, Y., 2015. Seismotectonics of southern Haiti: a new faulting model for the 12 January 2010 M7. 0 earthquake, *Geophys. Res. Lett.,* **42,** doi:10.1002/2015GL065505.

Sato, T. & Hirasawa, T., 1973. Body wave spectra from propagating shear cracks, *J. Phys. Earth,* **21,** 415–431.

Scherer, J., 1912. Great earthquakes in the Island of Haiti, *Bull. seism. Soc. Am.,* **2,** 161–180.

Shi, Z. & Day, S.M., 2013. Rupture dynamics and ground motion from 3-D rough fault simulations, *J. geophys. Res.,* **118**(3), 1122–1141.

Shinozuka, M., 1988. State-of-the-art report: engineering modeling of ground motion, in *Proceedings of the 9th World Conference on Earthquake Engineering (9WCEE),* Tokio, Japan, 2–9 August 1988.

Somerville, P.G., Smith, N.F., Graves, R.W. & Abrahamson, N.A., 1997. Modification of empirical strong ground motion attenuation relations to include the amplitude and duration effects of rupture directivity, *Seismol. Res. Lett.,* **68,** 199–222.

Spudich, P. & Frazer, L.N., 1984. Use of ray theory to calculate high-frequency radiation from earthquake sources having spatially variable rupture velocity and stress drop, *Bull. seism. Soc. Am.,* **74,** 2061–2082.

Stein, R.S., Barka, A.A. & Dieterich, J.H., 1997. Progressive failure on the North Anatolian fault since 1939 by earthquake stress triggering, *Geophys. J. Int.,* **128,** 594–604.

St Fleur, S. *et al.*, 2016. Site effects in Port-au-Prince (Haiti) from the analysis of spectral ratio and numerical simulations, *Bull. seism. Soc. Am.,* **106,** 1298–1315.

Symithe, S. & Calais, E., 2016. Present-day shortening in Southern Haiti from GPS measurements and implications for seismic hazard, *Tectonophysics,* **679,** 117–124.

Symithe, S.J., Calais, E., Haase, J.S., Freed, A.M. & Douilly, R., 2013. Coseismic slip distribution of the 2010 M 7.0 Haiti Earthquake and resulting stress changes on regional faults, *Bull. seism. Soc. Am.,* **103,** 2326–2343.

Terrier, M., Bialkowski, A., Nachbaur, A., Prépetit, C. & Joseph, Y.F., 2014. Revision of the geological context of the Port-au-Prince metropolitan area, Haiti: implications for slope failures and seismic hazard assessment, *Nat. Hazards Earth Syst. Sci.,* **14,** 2577–2587.

Wald, D.J. & Heaton, T.H., 1994. Spatial and temporal distribution of slip for the 1992 Landers, California, earthquake, *Bull. seism. Soc. Am.,* **84**(3), 668–691.

Wells, D.L. & Coppersmith, K.J., 1994. New empirical relationships among magnitude, rupture length, rupture width, rupture area, and surface displacement, *Bull. seism. Soc. Am.,* **84**(4), 974–1002.

Wessel, P. & Smith, W.H., 1998. New, improved version of generic mapping tools released, *EOS, Trans. Am. geophys. Un.,* **79,** 579–579.

Wright, T.J., Lu, Z. & Wicks, C., 2004. Constraining the slip distribution and fault geometry of the M_w 7.9, 3 November 2002, Denali fault earthquake with interferometric synthetic aperture radar and global positioning system data, *Bull. seism. Soc. Am.,* **94**(6B), S175–S189.

SUPPORTING INFORMATION

Supplementary data are available at *GJI* online.

Figure S1. Spatial distribution of peak ground velocity (PGV) in the fault-normal direction obtained from dynamic rupture simulations on a south-dipping fault. The black star shows the epicentre location, the white triangles mark the location of selected stations and the colour gradient characterizes the magnitude of the peak horizontal ground velocity.

Figure S2. Spatial distribution of peak ground velocity (PGV) in the fault-parallel direction obtained from dynamic rupture simulations on a south-dipping fault. The black star shows the epicentre location, the white triangles mark the location of selected stations and the colour gradient characterizes the magnitude of the peak horizontal ground velocity.

Table S1. Mean and standard deviation values of PGA (g) for all stations listed in Table 1 obtained by combining low- (scenarios DA1, DB1, VA1, VB2, VA2 and DB2) and high-frequency (uniform-size subevent distribution) simulation results.

Table S2. Mean and standard deviation values of PGA (g) for all stations listed in Table 1 obtained by combining low- (scenarios DA1, DB1, VA1, VB2, VA2 and DB2) and high-frequency (variable-size subevent distribution) simulation results.

Please note: Oxford University Press is not responsible for the content or functionality of any supporting materials supplied by the authors. Any queries (other than missing material) should be directed to the corresponding author for the paper.